

DNS OF HIGH TEMPERATURE EFFECTS ON COMPRESSIBLE ISOTROPIC TURBULENCE

A THESIS

submitted by

GOKUL RAMANATHAN

for the award of the degree

of

MASTER OF SCIENCE



**DEPARTMENT OF AEROSPACE ENGINEERING
INDIAN INSTITUTE OF TECHNOLOGY MADRAS.**

SEPTEMBER 2017

THESIS CERTIFICATE

This is to certify that the thesis titled **DNS OF HIGH TEMPERATURE EFFECTS ON COMPRESSIBLE ISOTROPIC TURBULENCE**, submitted by **Gokul Ramanathan**, to the Indian Institute of Technology, Madras, for the award of the degree of **Master of Science**, is a bona fide record of the research work done by him under our supervision. The contents of this thesis, in full or in parts, have not been submitted to any other Institute or University for the award of any degree or diploma.

Research Advisor
Dr. Shankar Ghosh
Assistant Professor
Dept. of Aerospace Engineering
IIT Madras, 600 036

Place: Chennai

Date: 4th September 2017

ACKNOWLEDGEMENTS

First and foremost, I would like to offer my sincerest gratitude to my thesis advisor Prof. Shankar Ghosh, who has supported me throughout my Master's study with his patience and knowledge whilst allowing me the room to work in my own way. He introduced me to the fascinating world of computational turbulence. I attribute the level of my Master's degree to his encouragement and effort. He has taught me literally everything that I know not just about fluid dynamics, but also the science and art of research. I hope to carry forward the sense of ethics, hard-work, perseverance and professionalism that he has very patiently tried to instil in me. He has set such an exemplary path that I know when I receive the opportunity to guide someone with my knowledge in the future, I will do so with the humility that I have extremely big shoes to fill.

I wish to thank the members of my general test committee, Prof. Amit Kumar and Prof. T. N. C. Anand for the useful discussions and feedback they have provided throughout my research.

I would like to thank my lab mates, specifically Mr. Jerry Samuel, Mr. Prakash Thirunavukkarasu and Mr. Pawan Kerkar for their constructive criticism and support. I would also like to mention my friends Mr. Joel Varun Vasanth, Mr. Suraj Singh, Mr. Aritra Chakraborty, Mr. Aditya Prajapati, Mr. Abhishek Sivaram and Ms. Anjali Ramesh for their support and encouragement during testing times.

I am thankful for an extremely supportive family. I dedicate this work to my mother, Dr. Kalyani Krishnan who is the epitome of everything that is good about this world. Her constant effort in the background is what motivates me to put my best foot forward in the foreground.

The computational resources required for this work are provided by the P. G. Senapathy Center for Computing Resources and the Department of Aerospace Engineering at the Indian Institute of Technology Madras, Chennai, India.

ABSTRACT

KEYWORDS: compressible isotropic turbulence ; high temperature effects; direct numerical simulation; turbulence; computational fluid dynamics.

DNS is used to study high temperature effects on compressible isotropic turbulence. Local thermodynamic equilibrium (L.T.E.) conditions are assumed to apply as the time scales for chemical equilibration are typically much smaller compared to the turbulence time scales. Four different physical models for air are proposed. Model 1 assumes air to be a calorically and thermally perfect gas. Constant specific heats are assumed. The transport properties are computed using a simple algebraic dependence on temperature. Models 2, 2a and 2b account for various aspects of high temperature effects on compressible isotropic turbulence. Effects of both thermodynamic and transport properties are studied using model 2. These effects are then decoupled and studied individually through models 2a and 2b. For model 2a the thermodynamic properties for air are obtained using the LTE based model while the transport properties are computed as in model 1. The reverse is done for model 2b. These LTE based models fall back upon model 1 at low temperatures.

A fully parallel compressible pseudo-spectral solver is developed for the simulations. The solver uses Fourier spectral methods for spatial discretization. A skew-symmetric form of representation of the non-linear terms is implemented to reduce aliasing errors. Oddball wavenumber filtering is used to reduce spurious buildup of energy in the smaller length scales for even number of grid points. A fourth order explicit Runge-Kutta method is used for time advancement. The flow solver is parallelized using MPI and validated using several benchmark problems.

Three different methods for initialization of an isotropic turbulent flow-field have been compared. The method by Ristorcelli and Blaisdell (1997) is found to be the most appropriate at high temperatures as it has an accurate estimate for the initial values of all the fluctuating quantities.

Comparison of models 1 and 2b highlight the effects of L.T.E. based transport properties at high temperatures. Turbulent kinetic energy (q^2) is found to decay faster for model 1 than for model 2b initially. However after some time, the decay is stronger for model 2b. Turbulent dissipation ϵ , combined with the values of $\bar{\mu}$ for the two models explains this behaviour. The energy spectra for both the models show larger dispersion of energy across the smaller length scales for model 2b in comparison to model 1.

Comparison of models 1 and 2a highlight the effects of L.T.E based thermodynamic properties at high temperatures. Turbulent kinetic energy is found to decay faster for model 2a than for model 1. The flow dilatation for model 2a is found to be an order of magnitude stronger than that for model 1. The time evolution of turbulent dissipation coupled with the fact that $\bar{\mu}$ remains more or less the same for both the models gives us the q^2 decay behaviour observed in this case. The energy spectra for both the models show larger dispersion of energy across the smaller length scales for model 2a in comparison to model 1.

Comparison of models 1 and 2 highlight the cumulative effects of both L.T.E based thermodynamic and transport properties. Time evolution of dilatation for model 2 is similar to that of model 2a and time evolution of enstrophy, turbulent kinetic energy and dissipation is similar to that of model 2b. The energy spectra show larger dispersion of energy across the smaller length scales for model 2 than for model 1.

Time evolution of mean internal energy shows that the internal energy content for models 2a and 2 are much more when compared to those for models 1 and 2b. This is because for models 2a and 2, L.T.E. based thermodynamic properties are used.

Both the Taylor microscale λ and Kolmogorov scale η are found to decrease slightly first and then increase at a constant rate. Their ratio λ/η , which is representative of the range of length scales in the flow-field decreases with time. This ratio decreases for model 2 to 2b to 2a to 1.

As model 2 combines the effects of both thermodynamic and transport properties, it is suggested as the most appropriate model for simulation of compressible isotropic turbulence at high temperatures.

TABLE OF CONTENTS

ACKNOWLEDGEMENTS	i
ABSTRACT	ii
LIST OF TABLES	vi
LIST OF FIGURES	viii
ABBREVIATIONS	ix
NOTATION	x
1 Introduction	1
1.1 Motivation and background	1
1.2 Review of past work	1
1.2.1 Theoretical work	2
1.2.2 Experimental work	3
1.2.3 Computational work	4
1.3 Overview	6
2 Simulation Methodology	10
2.1 Governing Equations	10
2.2 Physical Models	12
2.2.1 Model 1	12
2.2.2 Model 2	13
2.3 Numerical method	15
2.3.1 Spatial Discretization	15
2.3.2 Time Advancement	18
2.4 Solution Algorithms	18
2.5 Flow solver validation	21
2.6 Solver Parallelization	24

3	Initial conditions	27
3.1	Rogallo's method	27
3.2	Erlebacher et. al.'s method	29
3.3	Ristorcelli and Blaisdell method	32
3.4	Comparison of initial conditions	34
4	Results and discussion	38
4.1	Flow-field initialization	38
4.2	Low temperature simulation	38
4.3	High temperature simulation	39
4.3.1	Comparison between models 1 and 2b	39
4.3.2	Comparison between models 1 and 2a	44
4.3.3	Comparison between models 1 and 2	47
4.4	Length scales for isotropic turbulence at high temperatures	51
5	Summary	54

LIST OF TABLES

2.1	Reference quantities at 300K used for non-dimensionalisation . . .	11
2.2	Various high temperature effects and temperatures beyond which they are significant.	13
2.3	Periodic shock tube problem: comparison of present simulation values with analytical solution. ρ_1 and ρ_2 denote density values behind the shock wave and the contact discontinuity respectively, T_1 and T_2 are the maximum and minimum temperatures and U denotes the maximum streamwise velocity magnitude.	22
3.1	Comparison of initial values of parameters for the simulations at 300K. All values have been non-dimensionalized with model 1 values at 300K. 34	
4.1	Comparison of initial values of flow parameters for simulations at 15000K for models 1 and 2b. All values have been non-dimensionalized suitably with Model 1 values at 300K with the exception of Re_λ	39
4.2	Comparison of initial values of flow parameters for simulations at 15000K for models 1 and 2a. All values have been non-dimensionalized suitably with Model 1 values at 300K, with the exception of Re_λ	45
4.3	Comparison of initial values of flow parameters for simulations at 15000K for models 1 and 2. All values have been non-dimensionalized suitably with Model 1 values at 300K, with the exception of Re_λ	49

LIST OF FIGURES

2.1	Variation of (a) internal energy $e(J/kg)$ and (b) dynamic viscosity coefficient $\mu(kg/ms)$ with temperature for models 1 and 2. ——— represents model 1 and ———— represents model 2.	13
2.2	Schematic to illustrate aliasing. Wave numbers n and m on being added become $n + m$. As this wavenumber lies outside the range of the computational domain, represented from $-N/2$ to $N/2 - 1$, it is aliased to $n + m - N$. Thus, aliasing causes a build up of energy in low wavenumbers.	16
2.3	A schematic showing periodic shocktube problem.	21
2.4	Instantaneous profiles of ρ , p , T and u after one non-dimensional time unit. ——— represent Ghosh et. al. (2008) and ■ represent calculated results.	21
2.5	Pressure contours for vortex convection problem at (a) $t = 0$, (b) $t = 0.25$, (c) $t = 0.5$ and (d) $t = 0.75$ and (e) $t = 1$	23
2.6	Shows the time evolution of Re_λ . ■ denotes Blaisdell (1990) and ——— denotes simulation result.	24
2.7	Schematic showing (a) distribution of processors and (b) data transfer for fft along y and z coordinate directions respectively.	24
2.8	Instantaneous profiles of ρ , p , T and u after one non-dimensional time unit. ——— represent serial solver and ■ represent parallel solver.	25
3.1	Comparison of turbulence statistics between three different isotropic turbulence initialization methods: (a) velocity derivative skewness s , (b) q^2/q_0^2 , (c) $\overline{T'^2}$ and (d) χ . ——— denotes Ristorcelli and Blaisdell (1997), ———— denotes Erlebacher et. al. (1991) and —·—·—·— denotes Rogallo (1981).	35
4.1	Comparison of (a) turbulent kinetic energy and (b) vorticity between models 1 and 2 at 300K. ——— denotes model 1 and ■ denotes model 2	39
4.2	Comparison of (a) q^2/q_0^2 and (b) ϵ between models 1 and 2b at 15000 K. ——— represents model 1 and —·—·—·— represents model 2b.	40
4.3	Comparison of (a) $\overline{\theta'^2}$ and (b) $\overline{\omega'^2}$ between models 1 and 2b at 15000K. ——— represents model 1 and —·—·—·— represents model 2b.	40
4.4	Enstrophy budgets: Comparison of (a) vortex stretching, (b) vortex dissipation, (c) enstrophy-dilatation interaction and (d) total right hand side of enstrophy transport equation between models 1 and 2b at 15000 K. ——— represents model 1 and —·—·—·— represents model 2b.	42

4.5	Comparison of energy spectra between models 1 and 2b at 15000K. —— denotes the initial spectrum, ———— denotes the spectrum of model 1 and - - - - - denotes the spectrum of model 2b at $t = 0.5$.	43
4.6	Comparison of (a) \bar{T} and (b) \bar{e} between models 1 and 2b at 15000 K. —— represents model 1 and - - - - - represents model 2b.	44
4.7	Comparison of (a) q^2/q_0^2 and (b) ϵ between models 1 and 2a at 15000 K. —— represents model 1 and - - - - - represents model 2a.	44
4.8	Comparison of (a) $\overline{\theta'^2}$ and (d) $\overline{\omega'^2}$ between models 1 and 2a at 15000K. —— represents model 1 and - - - - - represents model 2a.	45
4.9	Enstrophy budgets: Comparison of (a) vortex stretching, (b) vortex dis- sipation, (c) enstrophy-dilatation interaction and (d) total rate of enstro- phy evolution between models 1 and 2a at 15000 K. —— represents model 1 and - - - - - represents model 2a.	46
4.10	Comparison of energy spectra between models 1 and 2a at 15000K. —— denotes the initial spectrum, ———— denotes the spectrum of model 1 and the - - - - - denotes the spectrum of model 2a at $t = 0.5$.	47
4.11	Comparison of (a) \bar{e} for model 1 and (b) \bar{e} for model 2a at 15000K. —— represents model 1 and - - - - - represents model 2a.	48
4.12	Comparison of (a) q^2/q_0^2 and (b) ϵ between models 1 and 2 at 15000 K. —— represents model 1 and ———— represents model 2.	48
4.13	Comparison of (a) $\overline{\theta'^2}$ and (d) $\overline{\omega'^2}$ between models 1 and 2 at 15000K. —— represents model 1 and ———— represents model 2.	49
4.14	Enstrophy budgets: Comparison of (a) vortex stretching, (b) vortex dis- sipation, (c) enstrophy-dilatation interaction and (d) total rate of enstro- phy evolution between models 1 and 2 at 15000 K. —— represents model 1 and ———— represents model 2.	50
4.15	Comparison of energy spectra between models 1 and 2 at 15000K. —— denotes the initial spectrum, ———— denotes the spectrum of model 1 and - - - - - denotes the spectrum of model 2 at $t = 0.5$	51
4.16	Comparison of (a) \bar{e} for model 1 and (b) \bar{e} for model 2 at 15000K. —— represents model 1 and ———— represents model 2.	51
4.17	Comparison of (a) η and (b) λ for all models at 15000K. —— repre- sents model 1 and ———— represents model 2.	52
4.18	Comparison of (a) λ/η for all models and (b) λ/λ_0 , η/η_0 for models 1 and 2 at 15000K. For (a), —— represents model 1, - - - - - repre- sents model 2a, — - - - - represents model 2b and ———— represents model 2.	53

ABBREVIATIONS

DNS	Direct numerical simulation
LTE	Local thermodynamic equilibrium
TKE	Turbulent kinetic energy

NOTATION

C_p	non-dimensional specific heat at constant pressure
C_v	non-dimensional specific heat at constant volume
R	non-dimensional specific gas constant
M_t	turbulent Mach number
M_{t0}	initial turbulent Mach number
λ	non-dimensional Taylor microscale
Re_λ	Taylor microscale Reynolds number
u_i	non-dimensional velocity fluctuations
v_i	non-dimensional incompressible velocity fluctuations
w_i	non-dimensional compressible velocity fluctuations
ρ	non-dimensional density
p	non-dimensional pressure
T	non-dimensional temperature
μ	non-dimensional viscosity
κ	non-dimensional thermal conductivity
e	non-dimensional internal energy per unit mass
e_T	non-dimensional total energy per unit mass
K_t	non-dimensional coefficient to temperature gradient
c	non-dimensional speed of sound
u_i^*	dimensional velocity fluctuations
ρ^*	dimensional density
p^*	dimensional pressure
T^*	dimensional temperature
μ^*	dimensional viscosity
κ^*	dimensional thermal conductivity
c_0^*	background speed of sound
c_R^*	dimensional reference speed of sound
ρ_R^*	dimensional reference density
p_R^*	dimensional reference pressure
T_R^*	dimensional reference temperature
μ_R^*	dimensional reference viscosity
κ_R^*	dimensional reference thermal conductivity
C_p^*	dimensional specific heat at constant pressure
C_v^*	dimensional specific heat at constant volume
R^*	dimensional specific gas constant
$C_{p,R}^*$	dimensional reference specific heat at constant pressure
$C_{v,R}^*$	dimensional reference specific heat at constant volume
R_R^*	dimensional reference specific gas constant
T_c	critical temperature
ρ'	density fluctuations
p'	pressure fluctuations

T'	temperature fluctuations
Re	computational Reynolds number
Pr	Prandtl number
Pr_0	Prandtl number based on dimensional background values
γ	specific heats ratio
x, y, z	Cartesian coordinate directions
x_i, y_j, z_k	Cartesian grid coordinates
N_i	number of grid points along i^{th} directions
L_i	non-dimensional domain length
$f_{i,j,k}$	discrete representation of $f(x, y, z)$
$\hat{f}_{i,j,k}$	Fourier coefficients of $f_{i,j,k}$
\vec{k}	wavenumber vector
k_x, k_y, k_z	wavenumber along coordinate directions
k	wavenumber magnitude
\vec{r}	position vector in physical space
p	imaginary unit $\sqrt{-1}$
E	flux term
Δt	time step
$\vec{e}_1, \vec{e}_2, \vec{e}_3$	unit vectors along x, y and z directions
\vec{u}	velocity vector in Fourier space
$E(k)$	energy spectrum
u^C	compressible velocity
u^I	incompressible velocity
p^I	incompressible pressure
χ	compressibility
ϵ	non-dimensional dissipation
d	dilatation
p_1, ρ_1, T_1	first order pressure, density and temperature fluctuations
s	mean velocity derivative skewness
q^2	non-dimensional turbulent kinetic energy
q_0^2	non-dimensional initial turbulent kinetic energy
$\overline{T'^2}$	non-dimensional mean square temperature fluctuations
$\overline{p'^2}$	non-dimensional mean square pressure fluctuations
$\overline{\rho'^2}$	non-dimensional mean square density fluctuations
$\overline{\theta'^2}$	non-dimensional mean square fluctuating divergence
$\overline{\omega'^2}$	non-dimensional mean square fluctuating vorticity
\overline{T}, \bar{e}	non-dimensional mean temperature and mean internal energy
ν	non-dimensional kinematic viscosity
η	non-dimensional kolmogorov scale

CHAPTER 1

Introduction

1.1 Motivation and background

Isotropic turbulence is the simplest form of turbulence where the turbulence statistics are direction independent. Owing to its simplicity, it is popular among researchers for studying the effects of physical and numerical models.

In general, the large scales of a turbulent flow-field are not isotropic, since they are determined by the particular geometrical features of the boundaries. However in 1941, Andrey Kolmogorov postulated that for very high Reynolds numbers, small scale turbulent motions are statistically isotropic. In the process of energy cascading, the geometric and directional information associated with the large scales of a turbulent flow-field is lost, rendering the statistics of the small scales to have a universal character. Thus, although isotropic turbulence is generally not observed directly in nature, small scale turbulence is statistically isotropic for all turbulent flows when the Reynolds number is sufficiently high.

In certain aerospace applications like localised energy deposition for flow control or the flow-field behind the bow shock of a re-entry vehicle, the temperatures associated with the flow are significantly high. If, for some reason the flow transitions, then the effects of these high temperatures on the turbulent flow-field would make an interesting study. The turbulence may not always be isotropic, but owing to its simplicity, isotropic turbulence is a good starting point for studying the physics of high temperature effects on turbulence.

1.2 Review of past work

Isotropic turbulence has been studied using theoretical, experimental and computational methods in detail in the past.

1.2.1 Theoretical work

Corrsin (1952) studied heat transfer in stationary isotropic turbulence under constant small temperature gradient and obtained an expression for the turbulent heat transfer coefficient which depends only on the velocity field. A corresponding correlation coefficient was also identified which depends only on velocity field and fluid physical properties. Kovasznay (1953) developed a first order perturbation theory for the compressible, viscous and heat conducting Navier-Stokes equations and showed that a fluid obeying these equations can have three distinct types of disturbance fields: the vorticity mode which occurs in an incompressible flow, the entropy mode which occurs through temperature fluctuations and acoustic mode which occurs in conventional acoustics. For small intensities of turbulence, these modes are independent. This theoretical work was extended by Chu and Kovasznay (1958), where a consistent higher order perturbation theory was presented with restrictions that assume the transport properties to be monotonic functions of temperature and a constant Prandtl number of 0.75. The higher order expansions were constructed based on expansion of disturbance fields in powers of an amplitude parameter. The non-linearity of the full Navier-Stokes equations was shown to be interpreted as interaction between the three basic modes. The main contribution of the paper was the outline of a consistent successive approximation for an arbitrary order in the amplitude parameter and the presentation of explicit formulae for the second order (bilateral) interaction between the modes. George (1992) proposed a theory for the decay of homogeneous, isotropic turbulence in which truly-self preserving solutions to the spectral energy equation were found that are valid at all scales of motion. The characteristic length scale was shown to be the Taylor microscale λ , which grows as the square root of time. This was consistent with the experimental results observed by George (1992) as discussed in section 1.2.2. Unlike the earlier efforts, however, the decay rate was shown to be of power law form, and to depend on the initial conditions so that the decay rate constants cannot be universal except possibly in the limit of infinite Reynolds number. Another consequence of the theory was that the velocity derivative skewness was found to increase during decay, at least until a limiting value was reached.

Multiple methods to understand and model the dissipation of compressible isotropic turbulence have been developed. Zeman (1991) developed an extension of second-order models for compressible isotropic turbulence and showed that two major terms con-

tribute to the compressibility of the flow-field: the dilatational dissipation and pressure-dilatation correlation. Additionally, the dilatational dissipation was modelled based on a shocklet dissipation theory of Zeman (1990) whereas the pressure-dilatation term was identified with the pressure fluctuation variance $\overline{p'^2}$. Erlebacher et. al. (1990) considered compressible turbulent flows, not restricted to compressible isotropic turbulence. They showed that contrary to the general belief that compressible flows at low M_t are almost incompressible, even if the divergence of the initial flow-field is small, it can grow rapidly on a non-dimensional time scale of the order of the fluctuating Mach number. They developed an asymptotic theory which describes the flow-field in terms of solenoidal and dilatational components and identified various compressible regimes with respect to the initial conditions. They also developed formulae that predict the level of compressibility in the flow-field after the initial transients had disappeared. The accuracy of these formulae were verified by direct numerical simulations of isotropic turbulence.

1.2.2 Experimental work

Batchelor and Townsend (1947) studied the decay of vorticity in isotropic turbulence. Measurements were made by analyzing electrically, the output from a hot-wire anemometer placed downstream from a grid in a uniform stream. The terms involved in the vorticity equation and their contribution in describing the rate of change of vorticity were discussed. Negative contribution to the rate of change of vorticity, given numerically by $d\overline{\omega'^2}/dt$, was found to arise from the viscosity, while a positive contribution was produced by the tendency for the random diffusive motion of fluid particles to extend vortex lines, a phenomenon otherwise known as vortex stretching. The Taylor microscale squared, denoted by λ^2 was found to increase approximately linearly with time during the decay of the turbulence and their rate of change was found to be consistent with the energy equation. Comte-Bellot and Corrsin (1965) found that when the average kinetic energies of normal velocity components in decaying, grid-generated turbulence are equilibrated by a symmetric contraction of the wind tunnel, this equality can persist downstream. An expression for the best power law fit to the inverse turbulent kinetic energy during the early part of the decay for rod and disk based experimental grid setups was also found.

Tavoularis et. al (1978) studied the effect of velocity derivative skewness for a wide range of Taylor Reynolds numbers and found it to increase with decreasing Reynolds numbers. This trend was found for $150 \leq Re_\lambda \leq 4$. However, experiments covering the range $4 \leq Re_\lambda \leq 1$ showed a maximum of Re_λ between 4 and 3 and a rapid decrease for $Re_\lambda < 2$.

Recently, efforts were taken by Aliseda et. al. (2014) to study homogenous isotropic slowly-decaying turbulence in a giant grid-wind tunnel setup. This was done to create a database and probe the smallest scales of isotropic turbulence with very high Reynolds numbers. To achieve this a very large wind tunnel was constructed with a giant inflatable grid to conceive slowly decaying homogenous isotropic turbulence in a large region of the test section. Measurements using a wide range of techniques including hot-wire anemometry, ultrasound anemometry, resonant cantilever anemometry, fast pitot tube anemometry and high-speed particle tracking were undertaken. Re_λ was estimated to be between 400 and 800, with Kolmogorov scales of the order of a few mm.

1.2.3 Computational work

One of the earliest comprehensive study of compressible isotropic turbulence using direct numerical simulation (DNS) was by Blaisdell (1990). Results for a variety of initial conditions show that the compressibility effects are highly dependent on the initial conditions. Thus, it is very difficult to model decaying compressible isotropic turbulence. This dependence can be understood from a linearization of the Navier-Stokes equations, which show that the solenoidal and dilatational fields are decoupled and thus have to be specified independently. Blaisdell (1990) also discussed theories that modelled the decay rates of turbulent kinetic energy in compressible isotropic turbulence and determined the effect of rms Mach number M_{rms} on the decay rate based on results by experimental measurements and theoretical work. Samtaney et. al. (2001) performed DNS of decaying compressible isotropic turbulence for a variety of initial conditions and for moderate M_t and Taylor microscale Reynolds numbers Re_λ and showed that the presence or absence of thermodynamic fluctuations and velocity divergence had a negligible effect on the decay of turbulent kinetic energy. The results of Blaisdell (1990) were also confirmed by showing that decaying compressible isotropic turbulence has no significant effect of M_t . Additionally an algorithm was discussed to extract shocklets from

turbulent flow-fields based on the probability density function of the shocklet strength. At moderate M_t , it was shown that the most probable shocklet strength is proportional to $\frac{M_t}{Re_\lambda}$. Ristorcelli and Blaisdell (1997) showed that for turbulence of a finite M_t , there is finite effect of compressibility. A methodology for generating initial conditions for fluctuating thermodynamic quantities consistent with finite M_t effects was presented. These initial conditions were shown to give rise to smooth development of flow in contrast to cases of initialization where the flow-fields are specified arbitrarily or set to zero.

Sarkar and Hussaini (1993) studied the sound generated by isotropic turbulence using hybrid direct numerical simulation (DNS) method. It was observed that the acoustic efficiency in the simulation of isotropic turbulence was substantially lesser than that in subsonic jet experiments. The dominant frequency of the computed acoustic pressure was found to be somewhat larger than the dominant frequency of the energy-containing scales of motion. The acoustic power in the simulations was proportional to ϵM_t^5 where ϵ is the turbulent dissipation rate and M_t is the turbulent Mach number.

Ghosh and Mahesh (2010) studied the thermal effects of laser-induced plasma on isotropic turbulence using DNS. Laminar and turbulent simulations were performed. For laminar simulations, a tear-drop shaped blast wave was found to propagate into the background becoming spherical in time. At short times, baroclinic vorticity was found to be generated as a consequence of propagation of the curved shock through the domain. At long times, the flow-field formed toroidal vortex rings, as observed in experiments. For turbulent simulations, turbulence levels were found to be enhanced in regions of compression across the blast wave and suppressed in regions of expansion in the plasma core.

Xinliang et. al. (2001) performed DNS of compressible isotropic turbulence at relatively high M_t and moderate Re_λ and studied the mechanics of shocklets. Dong Li et. al. (2013) studied temporal decorrelations in compressible isotropic turbulence using space-time correlation theory and DNS.

1.3 Overview

Most studies of isotropic turbulence assume air to be a calorically and thermally perfect gas. Internal energy is assumed to be a linear function of temperature. The specific heats at constant pressure and volume, denoted by C_p and C_v respectively, are assumed to be constant. The transport properties are monotonic functions of temperature. However, at high temperatures, air molecules undergo vibrational excitation and chemical reactions, altering the chemical composition of air. For instance at around 800K vibrational excitation become significant. Dissociation of various constituents of air can occur as temperature increases further. Oxygen and Nitrogen molecules undergo dissociation at around 2000K and 4000K respectively. At around 9000K ionization effects also start becoming significant. The thermodynamic and transport properties of air are significantly affected by these physical processes and can no longer be obtained from the calorically and thermally perfect gas model described earlier. Formation of charged species can have a prominent effect on transport properties of air like the coefficient of viscosity. Therefore in this work, decaying, compressible, isotropic turbulence is studied using different physical models for air to account for these high temperature effects. A cubic domain with side length 2π with specific initial values for parameters and turbulence statistics is allowed to decay naturally. The influence of high temperature effects on the evolution of turbulence statistics which include vorticity, divergence, turbulent kinetic energy and dissipation are studied through four physical models for air. Local Thermodynamic Equilibrium (L.T.E.) is assumed as the time scales associated with chemical equilibration are much smaller in comparison to the turbulence time scales. Model 1 assumes air to be a calorically and thermally perfect gas. It uses constant specific heats for computing thermodynamic properties while transport properties are computed using a power law for viscosity coefficients and a constant Prandtl number for the thermal conductivity coefficient. In model 2 high temperature effects on both thermodynamic and transport properties are accounted for by using a local thermodynamic equilibrium (L.T.E.) based approach. It has been observed that beyond around 10000K the L.T.E. based model predicts a sharp decrease in the coefficient of dynamic viscosity μ . This trend is in sharp contradiction to the prediction by model 1 which shows a continuous increase with temperature. Thus, to decouple and study the individual effects of thermodynamic and transport properties two other models are suggested. Model 2a follows the

L.T.E based approach to compute thermodynamic properties whereas transport properties are computed using model 1. Model 2*b*, on the other hand assumes a calorically perfect model for the thermodynamic properties and the L.T.E model for the transport properties. Detailed descriptions of the various high temperature models can be found in Ghosh (2008) and has also been discussed in chapter 2 of this thesis.

The objectives of this work are:

- to develop a parallel compressible Navier-Stokes flow solver to accurately simulate and study high temperature decaying compressible isotropic turbulence,
- to develop different physical models for air to account for the various high temperature effects,
- to study the effects of thermodynamic properties on high temperature compressible isotropic turbulence,
- to study the effects of transport properties on high temperature compressible isotropic turbulence,
- to study the combined effects of thermodynamic and transport properties on high temperature compressible isotropic turbulence,
- to propose explanations for differences observed in the evolution of statistical quantities by the various physical models suggested.

The principal contributions of this work are:

- A fully parallel compressible Navier-Stokes flow solver is developed and validated using benchmark problems. Fourier spectral methods are used for spatial discretization. Non-linear terms are de-aliased using a skew-symmetric representation. A fourth order Runge-Kutta explicit time integration scheme is used for time advancement. The flow solver is parallelized using message passing interface (MPI).
- Four different physical models for air are suggested in this work to account for high temperature effects on compressible isotropic turbulence. Model 1 uses a constant specific heats based calorically perfect gas model for air which is commonly used to study isotropic turbulence in literature. Model 2 (Ghosh and Mahesh, 2008) uses an L.T.E based approach to take into account high temperature effects on compressible isotropic turbulence. Both thermodynamic and transport properties are obtained as functions of temperature. Models 2*a* and 2*b* are used to decouple and study the effects of thermodynamic and transport properties respectively on compressible isotropic turbulence.
- Three different initial conditions for isotropic turbulence have been implemented. The method by Rogallo (1981) assumes the initial flow-field to be divergence free. Initial thermodynamic fluctuations are set to zero. Erlebacher et. al. (1991) split the turbulent velocity fluctuations into compressible and incompressible parts.

Arbitrary spectrum and rms values can be assigned to the thermodynamic and velocity fluctuations. The compressibility in the flow-field can also be arbitrarily assigned. The method by Ristorcelli and Blaisdell (1997) is used to obtain a thermodynamic fluctuation field that is coupled to a weakly compressible velocity fluctuation field. The results from all three initialization methods are compared and the method by Ristorcelli and Blaisdell (1997) is chosen to be implemented to obtain the initial velocity and thermodynamic fluctuating field at high temperatures.

- Compressible isotropic turbulence simulation at 300K shows model 2 to provide exactly the same results as model 1. This is to be expected as at these temperatures, high temperature effects are absent and model 2 should fall back upon model 1.
- Compressible isotropic turbulence simulations are then conducted at 15000K using models 1, 2a, 2a and 2. The initial turbulent kinetic energy and computational Reynolds number are fixed across all model simulations. The initial energy spectrum used is a power four spectrum.
- Comparison of Models 1 and 2b highlight the effects of L.T.E. based transport properties at high temperatures.
 - Turbulent kinetic energy is found to decay faster for model 1 than for model 2b initially. However, after some time, the decay is stronger for model 2b.
 - The turbulent kinetic energy budget reveals turbulent dissipation to be the only non-negligible term. It is mainly comprised of solenoidal/vortical and dilatational components.
 - The enstrophy budget shows competing effects of vortex stretching and vortex dissipation that affect the magnitude of enstrophy in the flow-field. These effects are stronger for model 2b when compared to model 1.
 - This combined with the values of $\bar{\mu}$ for the two models explains the time evolution behaviour of turbulent kinetic energy.
 - The energy spectra for both the models show larger dispersion of energy across the smaller length scales for model 2b in comparison to model 1.
 - The range of mean internal energy is similar for both models. There is an increase in internal energy due to a decrease in turbulent kinetic energy.
- Comparison of Models 1 and 2a highlight the effects of L.T.E based thermodynamic properties at high temperatures.
 - Turbulent kinetic energy is found to decay faster for model 2a than for model 1.
 - Thermodynamic properties have a direct effect on flow dilatation. The dilatation is found to be an order of magnitude stronger for model 2a than model 1.
 - The turbulent kinetic energy budget reveals turbulent dissipation to be the only non-negligible term. Again, solenoidal dissipation is found to be much stronger than dilatational dissipation for both models.
 - The enstrophy budget shows that vortex stretching, viscous dissipation are predominant for both the models. A transient term, the enstrophy-dilatation interaction is found to exist for model 2a initially. The effect of this term is also visible in the initial time evolution of turbulent kinetic energy.

- This magnitude of $\bar{\mu}$ remains more or less same for both the models throughout the duration of the simulation.
- The mean internal energy for model 2a \bar{e} is approximately ten times that of model 1 throughout the duration of the simulation.
- The energy spectra for both the models show larger dispersion of energy across the smaller length scales for model 2a in comparison to model 1.
- Comparison of Models 1 and 2 highlight the cumulative effects of both L.T.E based thermodynamic and transport properties.
 - Time evolution of dilatation is similar to that of model 2a and time evolution of enstrophy is similar to that of model 2b.
 - Turbulent kinetic energy is found to decay faster for model 1 than for model 2 initially. However, after some time, the decay is stronger for model 2. This is similar to q^2 time evolution observed when Models 1 and 2b are compared.
 - Turbulence dissipation comparison is also similar to that between Models 1 and 2b. Effects of vortex stretching, vortex dissipation and enstrophy-dilatation interaction are found to be larger for model 2 than for model 1. While the effects of vortex stretching and dissipation for model 2 are similar to that of model 2b, the enstrophy-dilatation interaction transience is similar to that of model 2a.
 - The energy spectra show larger dispersion of energy across the smaller length scales for model 2 than for model 1. Model 2 has the highest energy per wave-number in the smaller length scales in comparison to all models.
 - Time evolution of mean internal energy shows that the internal energy content for Models 2 is approximately ten times that of model 1. This is similar to the internal energy comparison between models 2a and 1.
- Both the Taylor microscale λ and Kolmogorov scale η are found to decrease slightly first and then increase at a constant rate. Their ratio λ/η , which is representative of the range of length scales in the flow-field decreases with time. This ratio is the largest for model 2, followed by model 2b, then 2a and finally 1.
- Thus, dissipation is found to be affected by the transport properties and compressibility effects are found to be affected by the thermodynamic properties.
- The simulation results seem to suggest that model 2 which accounts for high temperature effects associated with both thermodynamic and transport properties should be chosen for simulating high temperature effects on decaying compressible isotropic turbulence accurately.

CHAPTER 2

Simulation Methodology

This chapter describes the simulation methodology used in this work. Turbulence is a multi-scale phenomenon and compressible isotropic turbulence requires that very fine length scales of the flow-field be resolved accurately. Also, there are no strong discontinuities in the flow-field. Thus, a spectral method is used for the purpose of spatial discretization. Time advancement is performed using explicit 4th order Runge-Kutta method. Various physical models for air are suggested to model high temperature effects. Details of the simulation methodology are discussed below.

2.1 Governing Equations

The governing equations are the unsteady, compressible Navier-Stokes equations. In non-dimensional form they are given as follows:

$$\begin{aligned}\frac{\partial \rho}{\partial t} + \frac{\partial}{\partial x_j}(\rho u_j) &= 0, \\ \frac{\partial}{\partial t}(\rho u_i) + \frac{\partial}{\partial x_j}(\rho u_i u_j) &= -\frac{\partial}{\partial x_j} \left[p \delta_{ij} - \frac{\mu}{Re} \left(\frac{\partial u_i}{\partial x_j} + \frac{\partial u_j}{\partial x_i} - \frac{2}{3} \frac{\partial u_k}{\partial x_k} \delta_{ij} \right) \right], \\ \frac{\partial}{\partial t}(\rho e_T) + \frac{\partial}{\partial x_j}(\rho e_T u_j) &= \frac{\partial}{\partial x_j} \left[-p u_j + \frac{\mu}{Re} \left(\frac{\partial u_i}{\partial x_j} + \frac{\partial u_j}{\partial x_i} - \frac{2}{3} \frac{\partial u_k}{\partial x_k} \delta_{ij} \right) u_i \right] \\ &\quad + \frac{\partial}{\partial x_j} \left(\frac{\mu}{(\gamma - 1) Re Pr} \frac{\partial T}{\partial x_j} \right),\end{aligned}\tag{2.1}$$

where,

$$\begin{aligned}x_i &= x_i^*/L_R^*, \quad u_i = u_i^*/c_R^*, \quad t = t^* c_R^*/L_R^* \\ \rho &= \rho^*/\rho_R^*, \quad p = p^*/\rho_R^* c_R^{*2}, \quad T = T^*/T_R^* \\ \mu &= \mu^*/\mu_R^*, \quad \kappa = \kappa^*/\kappa_R^*.\end{aligned}\tag{2.2}$$

In the above equations, ‘*’ is used to denote dimensional variables and the subscript ‘R’ denotes reference values. The reference values are evaluated at 300K. L_R^* is a reference lengthscale and c_R^* is the reference speed of sound. All other symbols have their usual meanings.

The total energy per unit mass e_T is given by

$$e_T = e + \frac{1}{2}u_i u_i \quad (2.3)$$

The equation of state upon non-dimensionalisation becomes

$$p = \rho T / \gamma \quad (2.4)$$

The non-dimensional parameters in the above set of equations are the Reynolds number Re given by

$$Re = \rho_R^* c_R^* L_R^* / \mu_R^*, \quad (2.5)$$

and the Prandtl number Pr is given by

$$Pr = \mu^* c_p^* / k^*. \quad (2.6)$$

T_R^*	c_R^*	ρ_R^*	R_R^*	$c_{V,R}^*$	$c_{P,R}^*$	μ_R^*
300K	347.28m/s	1.2kg/m ³	287.15J/kgK	717.85J/kgK	1005.025J/kgK	1.983×10^{-5} kg/ms

Table 2.1: Reference quantities at 300K used for non-dimensionalisation

The reference values used for the non-dimensionalisation shown in equation 2.2 are provided in table 2.1. It is important to note that the magnitude of L_R^* is problem dependent. κ_R^* is obtained from equation 2.6 given by

$$\kappa_R^* = \mu_R^* c_{p,R}^* / Pr, \quad (2.7)$$

where the reference quantities on the right hand side of the equation are obtained from table 2.1 and $Pr = 0.7$.

It has been assumed that

- the fluid is a continuum,
- radiation effects are negligible,
- the fluid is Newtonian in nature and bulk viscosity is negligible.
- local thermodynamic equilibrium (L.T.E.) conditions are valid.

Air is chosen as the fluid medium and different physical models are proposed for the same.

2.2 Physical Models

2.2.1 Model 1

For model 1, air is considered to be a calorically perfect ideal gas. Therefore the properties of air are calculated based on a constant specific heats model. The non-dimensional equation of state in this case is simply given by

$$P = \rho T / \gamma. \quad (2.8)$$

The internal energy e is related to temperature non-dimensionally by

$$e = \frac{T}{\gamma(\gamma - 1)}, \quad (2.9)$$

where γ for air is 1.4. The coefficient of viscosity is obtained from the non-dimensional power law

$$\mu = T^{0.67}. \quad (2.10)$$

$Pr = 0.7$ is used. Also, K_t is defined as the coefficient of the temperature gradient in equation 2.1. It is given by

$$K_t = \frac{\mu}{(\gamma - 1)RePr}. \quad (2.11)$$

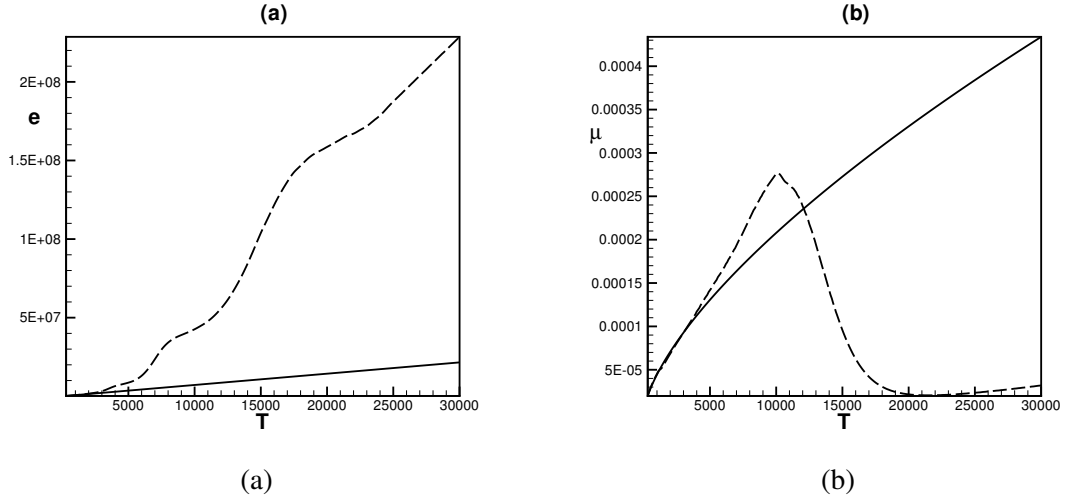


Figure 2.1: Variation of (a) internal energy $e(J/kg)$ and (b) dynamic viscosity coefficient $\mu(kg/ms)$ with temperature for models 1 and 2. — represents model 1 and - - - - represents model 2.

2.2.2 Model 2

Effect	T_c
Vibrational excitation	800 K
Dissociation of O_2	2000 K
Dissociation of N_2	4000 K
Ionization	9000 K

Table 2.2: Various high temperature effects and temperatures beyond which they are significant.

At standard temperature and pressure (STP) conditions, air can be assumed to behave as an ideal gas. The internal energy of a gas under such conditions predominantly consists of contributions from the translational and rotational energy modes. They are considered to be in equilibrium with each other and there is negligible contribution from the other modes. However at higher temperatures, contributions from vibrational and electronic excitation modes to the internal energy also becomes significant. Also the effects of chemical reactions like dissociation and ionization need to be considered. Table 2.2 shows the various phenomena and the critical temperatures T_c beyond which they significantly affect the thermodynamic and transport properties of air. Thus, model 2 takes into account these high temperature effects resulting from multiple internal energy modes and the dissociation and ionization of different species. The equation of state for model 2 is given by

$$P = \rho R(T)T, \quad (2.12)$$

where $R(T) = R^*(T)/(\gamma R_0^*)$. The thermodynamic and transport properties are obtained using a 11 species air model consisting of N_2 , O_2 , NO , N , O , N_2^+ , O_2^+ , NO^+ , N^+ , O^+ and e^- . At L.T.E., each of these species are individually in equilibrium. Thus, the equilibrium composition can be obtained from the law of mass-action. Once the equilibrium composition is obtained the thermodynamic and transport properties of air can be determined by minimization of Gibbs free energy, along with the use of mass conservation and electrical neutrality equations (Boulos et. al. 1994).

The effect of radiation has been neglected in this model. K_t takes on the form

$$K_t = \frac{\kappa}{RePr_0(\gamma - 1)}, \quad (2.13)$$

where Pr_0 is the Prandtl number based on the dimensional background values and has a value of 0.7.

Figure 2.1 shows plots of internal energy e and the coefficient of dynamic viscosity μ as a function of temperature at atmospheric pressure for models 1 and 2. All quantities are dimensional. Model 1 assumes a linear relationship between internal energy and temperature. Model 2 agrees with model 1 till around 2000K. But at higher temperatures, the two models differ significantly. For instance, at around 12000 K, internal energy as predicted by model 2 is about five times that of model 1 as shown in figure 2.1a. So at higher temperatures, a calorically perfect gas model is clearly insufficient to accurately represent the flow conditions. This statement is further supported by the variation of dynamic viscosity with temperature for both the models as shown in figure 2.1b. While model 1 assumes a power law for increase of viscosity with temperature, Model 2 shows a sharp decrease in viscosity with increase in temperature beyond 10000K (approximately). It is important to note that even other models for viscosity like Sutherland's model (Sutherland 1893) do not predict this decrease in viscosity with increase in temperature. The coefficient of thermal conductivity κ also shows similar discrepancies from κ values used for model 1. Hence, the effects of transport properties on decaying isotropic turbulence at high temperatures should by itself be very interesting. So, the effects of thermodynamic and transport properties should be decoupled and

studied separately. With this in mind, model 2 has further been subdivided into models 2a and 2b. In model 2a, thermodynamic properties are calculated based on L.T.E. while transport properties are obtained from model 1. On the other hand, for model 2b, only the transport properties are obtained from the high temperature model while the thermodynamic properties given by the calorically perfect gas model are used.

2.3 Numerical method

2.3.1 Spatial Discretization

A pseudo-spectral based fully parallel compressible Navier-Stokes flow solver has been developed to study this problem. A uniform Cartesian grid can be defined as

$$\begin{aligned} x_i &= \frac{i-1}{N_x} L_x & i &= 1, \dots, N_x, \\ y_j &= \frac{j-1}{N_y} L_y & j &= 1, \dots, N_y, \\ z_k &= \frac{k-1}{N_z} L_z & k &= 1, \dots, N_z, \end{aligned} \quad (2.14)$$

where N_i and L_i denote the number of grid points and length of domain respectively along the i direction. A function $f(x, y, z)$ can be represented on this cartesian grid in terms of a discrete fourier transform

$$f_{i,j,k} = \sum_{k_x=-N_x/2}^{N_x/2-1} \sum_{k_y=-N_y/2}^{N_y/2-1} \sum_{k_z=-N_z/2}^{N_z/2-1} \hat{f}_{k_x,k_y,k_z} e^{p(\vec{k} \cdot \vec{x})}, \quad (2.15)$$

where \vec{k} is the vector of wavenumbers whose components are k_x , k_y and k_z , \vec{x} is the position vector in physical space and p is the imaginary unit ($\sqrt{-1}$). The Fourier coefficients \hat{f}_{k_x,k_y,k_z} are given by

$$\hat{f}_{k_x,k_y,k_z} = \sum_{i=1}^{N_x} \sum_{j=1}^{N_y} \sum_{k=1}^{N_z} f_{i,j,k} e^{-p(\vec{k} \cdot \vec{x})}. \quad (2.16)$$

Spatial derivatives are then obtained in the Fourier space as

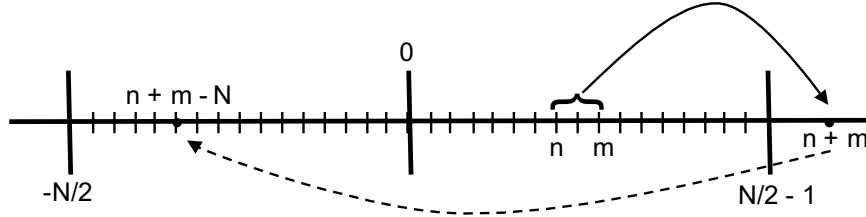


Figure 2.2: Schematic to illustrate aliasing. Wave numbers n and m on being added become $n + m$. As this wavenumber lies outside the range of the computational domain, represented from $-N/2$ to $N/2 - 1$, it is aliased to $n + m - N$. Thus, aliasing causes a build up of energy in low wavenumbers.

$$\frac{\widehat{\partial f}}{\partial x_\alpha} = p k_\alpha \hat{f}, \quad \frac{\widehat{\partial^2 f}}{\partial x_\alpha \partial x_\alpha} = -k_\alpha^2 \hat{f}. \quad (2.17)$$

Inverse Fourier transforms give spatial derivatives in the physical space.

In pseudo-spectral methods, products of quantities are taken in physical space. Consider two one dimensional functions $f(x)$ and $g(x)$ for the purpose illustration,

$$f(x) = \sum_{n=-\frac{N_x}{2}}^{\frac{N_x}{2}-1} \hat{f}_n e^{p k_n x}, \quad (2.18)$$

$$g(x) = \sum_{m=-\frac{N_x}{2}}^{\frac{N_x}{2}-1} \hat{g}_m e^{p k_m x}. \quad (2.19)$$

The product of the two functions is given by

$$f(x)g(x) = \sum_{n=-\frac{N_x}{2}}^{\frac{N_x}{2}-1} \sum_{m=-\frac{N_x}{2}}^{\frac{N_x}{2}-1} \hat{f}_n \hat{g}_m e^{p(k_n+k_m)x}. \quad (2.20)$$

When this product is discretized, some modes will have values of $(k_n + k_m)$ which lie outside the range of resolved wavenumbers, given by $\left[-\frac{2\pi}{L_x} \frac{N_x}{2} \dots \frac{2\pi}{L_x} \left(\frac{N_x}{2} - 1\right)\right]$, when N_x is even. These unresolved high wavenumber modes are aliased to resolved lower wavenumber modes. Figure 2.2 shows this process. This affects the derivatives of these products, given by

$$\left[\frac{\partial}{\partial x}(fg) \right]_j = \sum_{n=-\frac{N_x}{2}}^{\frac{N_x}{2}-1} \sum_{m=-\frac{N_x}{2}}^{\frac{N_x}{2}-1} p(k_n + k_m)^* \hat{f}_n \hat{g}_m e^{p(k_n + k_m)^* x}, \quad (2.21)$$

where $(k_n + k_m)^*$ denotes the wavenumber of the resolved mode to which $(k_n + k_m)$ is aliased. A skew symmetric representation of the derivatives of products given by

$$\frac{\partial}{\partial x}(fg) = \frac{1}{2} \left[\frac{\partial}{\partial x}(fg) + f \frac{\partial g}{\partial x} + g \frac{\partial f}{\partial x} \right] \quad (2.22)$$

is found to suppress aliasing errors (Blaisdell 1996). Hence the non-linear terms in the governing equation use this type of representation.

Since an even number of grid points are used across all simulations, Fourier modes that can be represented are in the range of $-N_i/2$ to $N_i/2 - 1$, where i denotes the Cartesian directions. Except for the $-N_i/2$ wavenumber, the other modes are in complex conjugate pairs. The unpaired wavenumber is referred to as the oddball wavenumber. Thus for a simulation in three dimensions, the oddball wavenumbers are $(k_x, k_y, k_z) = (N_x/2, k_y, k_z), (k_x, N_y/2, k_z), (k_x, k_y, N_z/2)$. These wavenumbers represent the three outside faces of the computational box in Fourier wave space. The Fourier coefficient of the oddball wavenumber mode is given by

$$\hat{f}_{-\frac{N_x}{2}} = \frac{1}{N_x} \sum_{j=1}^{N_x} f_j (-1)^j. \quad (2.23)$$

Thus for a real function $f(x)$, $\hat{f}_{-\frac{N_x}{2}}$ is real. Consider the derivative of a function $f(x)$ in Fourier space,

$$f'(x_j) = \sum_{n=-\frac{N_x}{2}}^{\frac{N_x}{2}-1} p k_n \hat{f}_n e^{i k_n x_j} + p k_{-\frac{N_x}{2}} \hat{f}_{-\frac{N_x}{2}}. \quad (2.24)$$

Since $f(x)$ is real, $f'(x)$ is also real. However, since $\hat{f}_{-\frac{N_x}{2}}$ is real, the second term of the above equation will have an imaginary part unless $\hat{f}_{-\frac{N_x}{2}}$ is set to zero. This occurs because the $n = \frac{N_x}{2}$ mode is also needed to correctly represent the derivative, but cannot be represented in the grid. Thus when using Fourier transforms to evaluate derivatives, it is necessary to set the oddball wavenumber Fourier coefficients to zero.

A computationally efficient version of the Discrete Fourier Transform (DFT) known as the Fast Fourier Transform (FFT) has been implemented using the FFTW library. Spectral methods offer exponential convergence and are thus desirable to study turbulence which has a large number of scales to resolve.

2.3.2 Time Advancement

For time advancement an explicit fourth order Runge-Kutta time integration scheme is used. It is a multistage scheme given by

$$\begin{aligned}
 u_i^{(1)} &= u_i^{(n)}, \\
 u_i^{(2)} &= u_i^{(n)} - \frac{\Delta t}{4} \left(\frac{\partial E}{\partial x} \right)^{(1)}, \\
 u_i^{(3)} &= u_i^{(n)} - \frac{\Delta t}{3} \left(\frac{\partial E}{\partial x} \right)^{(2)}, \\
 u_i^{(4)} &= u_i^{(n)} - \frac{\Delta t}{2} \left(\frac{\partial E}{\partial x} \right)^{(3)},
 \end{aligned} \tag{2.25}$$

where $u_i^{(n)}$ is the solution at the current time level and $\frac{\partial E}{\partial x}$ is the flux derivative term. $u_i^{(1)}$, $u_i^{(2)}$, $u_i^{(3)}$ and $u_i^{(4)}$ are the solutions at intermediate stages. Δt is the time step of the scheme. The solution at the $(n + 1)$ time level is given by

$$u_i^{(n+1)} = u_i^{(n)} - \Delta t \left(\frac{\partial E}{\partial x} \right)^{(4)}.$$

This is the modified form of the standard Runge-Kutta (Hoffmann and Chiang, 2000) formulation to reduce storage requirement.

2.4 Solution Algorithms

The solution procedure for the governing equations is slightly different for the different physical models. The different solution algorithms are listed below.

Model 1

- Initial values for u_i , p , ρ and T are specified based on the procedure of Ristorcelli and Blaisdell (1991) discussed in section 3.3.
- Internal energy e is obtained using 2.9 and e_T is computed from equation 2.3 and u_i computed from the previous step.
- Viscosity coefficient μ is obtained from equation 2.10.
- The right hand sides of the Navier-Stokes equations (equation 2.1) are computed using Fourier spectral derivatives.
- The solution is advanced in time. At the end of every time step, the velocities are updated as $u_i = \frac{\rho u_i}{\rho}$ and e is updated using the values of e_T in equation 2.3.
- Temperature T is updated by inverting equation 2.9.
- μ is updated using equation 2.10.
- K_t is updated using equation 2.11.
- Pressure field is updated using the equation of state 2.8.
- The procedure from step four onwards is repeated.

Model 2

- The initial values for u_i , p , ρ and T is as described for model 1.
- Internal energy e is obtained from L.T.E. based data using cubic spline interpolation for e vs T . An even spaced 300 point data is used between 0K and 30,000°K for the interpolation.
- e_T is computed from equation 2.3.
- $\mu(T)$, $\kappa(T)$ and characteristic gas constant R are obtained from the L.T.E based data for μ vs T (figure 2.1b), κ vs T and R vs T respectively using cubic spline interpolation.
- The right hand sides of the Navier-Stokes equations (equation 2.1) are computed using Fourier spectral derivatives.
- The solution is advanced in time. At the end of every time step, the velocities are updated as $u_i = \frac{\rho u_i}{\rho}$ and e is updated using the values of e_T in equation 2.3.
- Temperature T is updated by reverse interpolation through the L.T.E based data for e vs T (figure 2.1a).
- Characteristic gas constant R , viscosity coefficient μ and thermal conductivity κ are obtained from the L.T.E based data for R vs T , μ vs T (figure 2.1b) and κ vs T respectively using cubic spline interpolation.
- K_t is updated using equation 2.13.

- Pressure field is updated using equation of state 2.12.
- The procedure from step five onwards is repeated.

Model 2a

- The initial values for u_i , p , ρ and T is as described for model 1.
- Internal energy e is obtained from L.T.E. based data using cubic spline interpolation for e vs T .
- e_T is computed from equation 2.3.
- μ is obtained from equation 2.10. R is obtained from L.T.E. based data for R vs T using cubic spline interpolation.
- The right hand sides of the Navier-Stokes equations (equation 2.1) are computed using Fourier spectral derivatives.
- The solution is advanced in time. At the end of every time step, the velocities are updated as $u_i = \frac{\rho u_i}{\rho}$ and e is updated using the values of e_T in equation 2.3.
- Temperature T is updated by reverse interpolation through the L.T.E based data for e vs T (figure 2.1a).
- Characteristic gas constant R is obtained from L.T.E based data for R vs T using cubic spline interpolation and μ is obtained from equation 2.10.
- Pressure field is updated using equation of state 2.12.
- The process from step five onwards is repeated.

Model 2b

- The initial values for u_i , p , ρ and T is as described for model 1.
- Internal energy e is obtained using 2.9 and e_T is computed from equation 2.3 and u_i computed from the previous step.
- $\mu(T)$ and $\kappa(T)$ are obtained from the L.T.E based data for μ vs T (figure 2.1b) and κ vs T using cubic spline interpolation.
- The right hand sides of the Navier-Stokes equations (equation 2.1) are computed using Fourier spectral derivatives.
- The solution is advanced in time. At the end of every time step, the velocities are updated as $u_i = \frac{\rho u_i}{\rho}$ and e is updated using the values of e_T in equation 2.3.
- Temperature T is updated by inverting equation 2.9.
- μ and κ are obtained from the L.T.E based data for μ vs T (figure 2.1b) and κ vs T respectively using cubic spline interpolation.
- Pressure field is updated using the equation of state 2.8.
- The process from step four onwards is repeated.

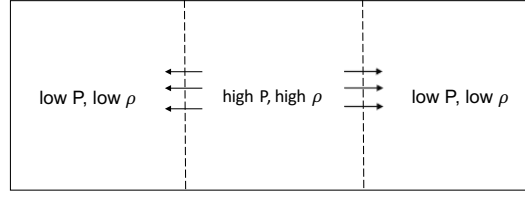


Figure 2.3: A schematic showing periodic shocktube problem.

2.5 Flow solver validation

This section describes validation studies that are performed on the flow solver. The flow solver has been validated using the periodic shock tube problem, vortex convection problem and decaying isotropic turbulence.

Periodic Shock Tube Problem

A tripartite domain is initialized with the middle portion at higher density and pressure in comparison to the adjacent portions. These regions are separated from each other by means of diaphragms. The density in the middle portion is 3.0 (non-dimensional) and 0.3 (non-dimensional) in the adjacent portions. The temperature is uniform throughout the domain at 1 (non-dimensional). Figure 2.3 shows a schematic for the problem. The non-dimensionalisation for the initial values has been discussed in section 2.1. Initially, the diaphragm dissolves instantaneously and the flow moves from high pressure region to the adjacent low pressure regions on either sides. The gradients are strong enough to produce shocks.

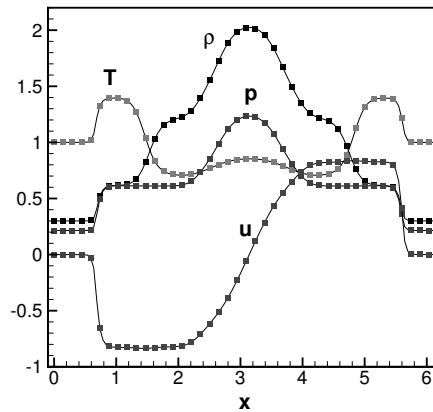


Figure 2.4: Instantaneous profiles of ρ , p , T and u after one non-dimensional time unit. — represent Ghosh et. al. (2008) and ■ represent calculated results.

Type	ρ_1	ρ_2	T_1	T_2	U
Solver	0.613	1.223	1.393	0.698	0.821
Ghosh and Mahesh	0.612	1.224	1.401	0.695	0.827
Calculated	0.614	1.221	1.401	0.704	0.824

Table 2.3: Periodic shock tube problem: comparison of present simulation values with analytical solution. ρ_1 and ρ_2 denote density values behind the shock wave and the contact discontinuity respectively, T_1 and T_2 are the maximum and minimum temperatures and U denotes the maximum streamwise velocity magnitude.

The plot obtained (figure 2.4) shows instantaneous profiles of density, temperature, pressure and velocity. The results have been compared against analytic solution for this problem (table 2.3) and those obtained by Ghosh and Mahesh (2005) (figure 2.4). The agreement in results is good. Even though the solver is three dimensional the problem validated here is one dimensional and along the x direction. In order to validate the solver in y and z directions the same one dimensional shock tube problem is initialized along these directions as well. The results obtained in all three directions are plotted and the agreement is satisfactory. This problem demonstrates the ability of the flow solver to resolve strong gradients.

Vortex Convection problem

The domain is initialized with a uniform flow and the vortex is superimposed over it at the center of the domain. The domain is 2 dimensional and of non-dimensional length 2π on each side with grid size of 128×128 . Periodic boundary conditions have been used in all directions. The vortex was initialized as follows

$$\begin{aligned}
u &= U_\infty \left(1 - \beta \frac{(y - y_c)}{R} e^{-\frac{r^2}{2}} \right), \\
v &= U_\infty \beta \frac{x - x_c}{R} e^{-\frac{r^2}{2}}, \\
T &= T_\infty - \frac{\left(\beta U_\infty e^{-r^2} \right)^2}{2c_p}, \\
\rho &= \rho_\infty \left(\frac{T}{T_\infty} \right)^{1/(\gamma-1)}, \\
r &= \frac{\sqrt{(x - x_c)^2 + (y - y_c)^2}}{R}.
\end{aligned} \tag{2.26}$$

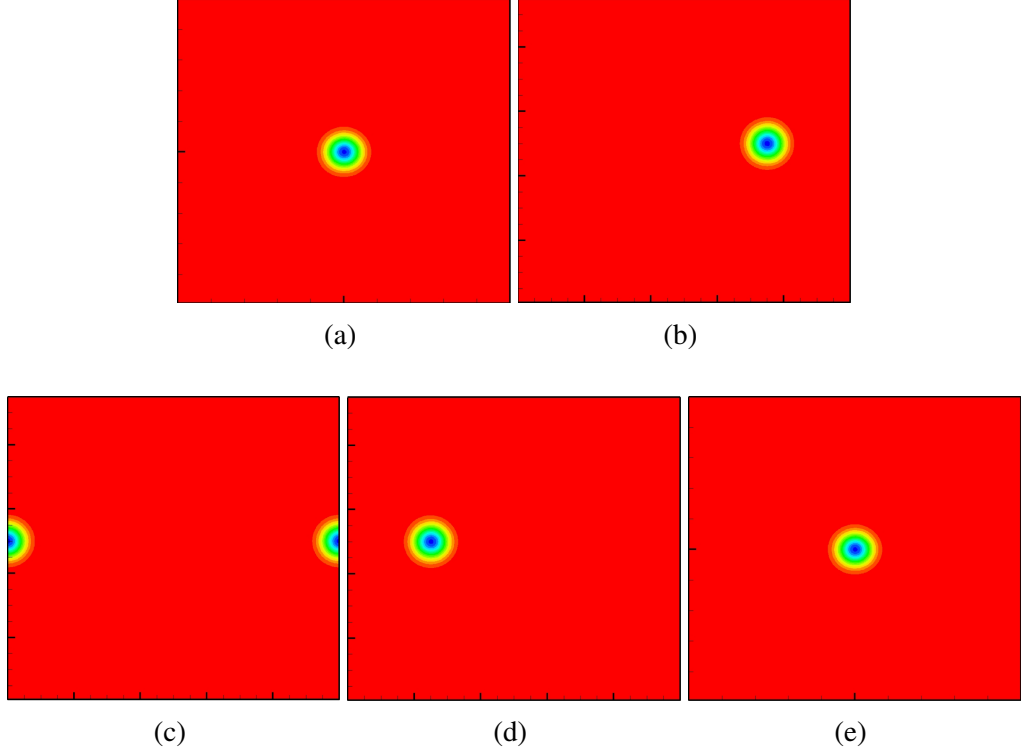


Figure 2.5: Pressure contours for vortex convection problem at (a) $t = 0$, (b) $t = 0.25$, (c) $t = 0.5$ and (d) $t = 0.75$ and (e) $t = 1$.

Here, $\beta = 0.02$, $R = 0.005$, $x_c = 1.57$ and $y_c = 3.14$. $T_\infty = 1$ is the background temperature and $\rho_\infty = 1$ is the free stream density. The free stream Mach number of the flow M_∞ is 2π and the free-stream pressure is computed as

$$p_\infty = \frac{\rho_\infty T_\infty}{\gamma} \quad (2.27)$$

As periodic boundary conditions are used, the vortex is convected back into the domain as it exits from the domain and reaches its initial position after one cycle. Pressure contours from the simulation shown in figure 2.5 demonstrate this. Note that the vortex is not getting distorted or dissipated indicating the low numerical dissipation and dispersion of the scheme. This problem demonstrates the ability of the flow solver to accurately simulate multi-dimensional problems.

Decaying isotropic turbulence

Decaying isotropic turbulence simulations were run on a three dimensional grid of size 96^3 . Temperature and pressure values are set to 1 and $1/\gamma$ (non-dimensional) uniformly throughout the domain, where γ is the ratio of specific heats. The flow field is initialized

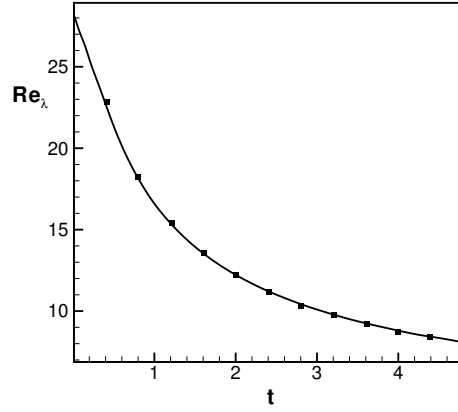


Figure 2.6: Shows the time evolution of Re_λ . ■ denotes Blaisdell (1990) and — denotes simulation result.

as per Rogallo (1981). As per this procedure, the velocity field is initialized with finite three dimensional incompressible fluctuations and the temperature, pressure and density fluctuating fields are assumed to be zero. A top-hat energy spectrum is used as the initial energy spectrum. The initial turbulent Mach number, M_{t0} is 0.3. The procedure to obtain the initial velocity field (Rogallo (1981)) has been discussed in detail in the next chapter (section 3.1). Taylor Reynolds numbers Re_λ with time is plotted and compared to DNS data of Blaisdell’s simulations (1990) (figure 2.6). The agreement with Blaisdell (1990) is good. This problem demonstrates the ability of the flow solver to simulated multi-scale three dimensional problems.

2.6 Solver Parallelization

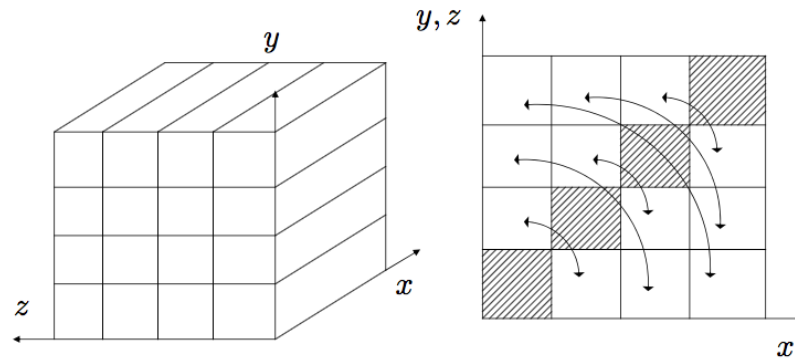


Figure 2.7: Schematic showing (a) distribution of processors and (b) data transfer for fft along y and z coordinate directions respectively.

DNS of turbulent flows is computationally expensive considering the need to resolve

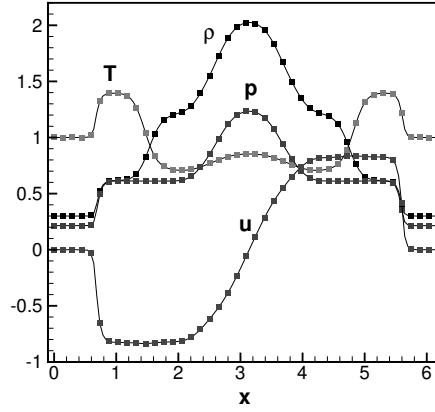


Figure 2.8: Instantaneous profiles of ρ , p , T and u after one non-dimensional time unit. — represent serial solver and ■ represent parallel solver.

a wide range of length and time scales. This requires extremely fine meshes leading to large memory consumption and long processing time which may not be feasible on a desktop computer. Moreover, spectral schemes are known to be computationally expensive given their ability to resolve wide range of length scales. Therefore, it is necessary to parallelize the solver so that it can be used for simulations on multiple machines simultaneously.

The solver is fully parallelized through domain decomposition technique using message passing interface (MPI). A pencil data structure is used to split the domain, where entire data along the x direction is available to all the processors while the data along y and z directions are equally distributed among the processors. This structure is shown in figure 2.7a. Fourier transforms along x direction are readily computed whereas transforms along any other directions require that the data be transposed prior to transforming.

The computation of the three dimensional Fourier transform is one of the very basic operations performed by the flow solver. Hence it is important that this operation is performed efficiently. Transforming data from the y and z directions to the x direction and back constitutes most of the processor time required to compute the Fourier transform. This transforming operation has been made efficient by breaking the data into cuboidal sections and transposing to the other end of the domain as shown in the figure 2.7b. The curved arrows show processors that exchange data with each other while the shaded processors exchange data within their own processors. The data is then suitably transposed within individual processors. The processors are synchronized in a way so that none of them are idle at any given time. Any communication between the proces-

sors is performed using MPI. To ensure that solver is accurately parallelized, results for the test problems specified in section 2.5 are compared with the serial solver. Figure 2.8 shows the comparison of the results for the shocktube problem between the serial and parallel solvers. They are confirmed to show good agreement.

CHAPTER 3

Initial conditions

In this chapter, three methods for initializing an isotropic turbulent flow-field are discussed. Subsequently they are compared and the best method to initialize a compressible isotropic turbulent flow-field at high temperatures is chosen.

3.1 Rogallo's method

This method was developed by Rogallo in (1981). According to this method, the initial flow field is assumed to be divergence free. The procedure to generate the initial turbulent flow-field is described below.

Let the unit vectors along x , y and z coordinate directions be given by \vec{e}_1 , \vec{e}_2 and \vec{e}_3 . As initial velocity field is divergence free, the velocity vectors in Fourier space, given by \hat{u} must lie in a plane that is perpendicular to wavenumber \vec{k} . Define a new set of unit vectors \vec{e}'_1 , \vec{e}'_2 and \vec{e}'_3 such that \vec{e}'_3 is parallel to \vec{k} . Thus \vec{e}'_3 can be given by,

$$\vec{e}'_3 = \frac{k_1\vec{e}_1 + k_2\vec{e}_2 + k_3\vec{e}_3}{k}, \quad (3.1)$$

where k_1 , k_2 and k_3 are components of \vec{k} , and k is the magnitude of this vector. The velocity vector in Fourier space based on the new set of unit vectors can then be given by

$$\hat{u} = \alpha k \vec{e}'_1 + \beta k \vec{e}'_2, \quad (3.2)$$

where $\alpha(k)$ and $\beta(k)$ are complex functions, given by

$$\alpha(k) = \left(\frac{E(k)}{4\pi k^2} \right)^{1/2} e^{i\theta_1} \cos(\phi), \quad \beta(k) = \left(\frac{E(k)}{4\pi k^2} \right)^{1/2} e^{i\theta_2} \sin(\phi), \quad (3.3)$$

where θ_1, θ_2 and ϕ_1 are random numbers between 0 and 2π and $E(k)$ is the energy spectrum. Multiple combinations of \vec{e}'_1 and \vec{e}'_2 are possible. To select one such combination Rogallo imposed the following condition

$$\vec{e}'_1 \cdot \vec{e}_3 = 0, \quad (3.4)$$

Then \vec{e}'_1 lies in the plane formed by \vec{e}_1 and \vec{e}_2 and can be written as

$$\vec{e}'_1 = \frac{A\vec{e}_1 + B\vec{e}_2}{(A^2 + B^2)^{1/2}} \quad (3.5)$$

where A and B are arbitrary constants. Since $\vec{e}'_1 \cdot \vec{e}_3 = 0$, equations 3.1 and 3.5 yield

$$B = -A \frac{k_1}{k_2}. \quad (3.6)$$

Subsequently \vec{e}'_1 is obtained as

$$\vec{e}'_1 = \frac{k_2\vec{e}_1 - k_1\vec{e}_2}{(k_1^2 + k_2^2)^{1/2}}. \quad (3.7)$$

Since unit vector $\vec{e}'_2 = \vec{e}'_1 \times \vec{e}_3$, it can be obtained as

$$\vec{e}'_2 = \vec{e}_1 \left[\frac{k_1 k_3}{k(k_1^2 + k_2^2)^{1/2}} \right] + \vec{e}_2 \left[\frac{k_2 k_3}{k(k_1^2 + k_2^2)^{1/2}} \right] - \vec{e}_3 \left[\frac{(k_1^2 + k_2^2)^{1/2}}{k} \right]. \quad (3.8)$$

Finally, the velocity vector in Fourier space is given by

$$\hat{u} = \vec{e}_1 \left[\frac{\alpha k k_2 + \beta k_1 k_3}{k(k_1^2 + k_2^2)^{1/2}} \right] + \vec{e}_2 \left[\frac{\beta k_2 k_3 - \alpha k k_1}{k(k_1^2 + k_2^2)^{1/2}} \right] - \vec{e}_3 \left[\beta \frac{(k_1^2 + k_2^2)^{1/2}}{k} \right], \quad (3.9)$$

where α and β are given by equation 3.3. The initial energy spectrum is a power four spectrum, given by

$$E(k) = 16 \left(\frac{2}{\pi} \right)^{1/2} \left(\frac{u_0^2}{k_0} \right) \left(\frac{k}{k_0} \right)^4 e^{-\left(\frac{k^2}{2k_0^2} \right)}, \quad (3.10)$$

where k_0 denotes the wavenumber at which the peak in the energy spectrum occurs. It's value is set to 5. u_0 is obtained from

$$\int_0^\infty E(k) dk = \frac{3}{2} u_0^2. \quad (3.11)$$

The above described procedure produces a three dimensional incompressible fluctuating velocity field of desired initial turbulent Mach number, M_{t0} . In order to obtain a realistic flow-field, the turbulence is allowed to decay over time. During this decay, the turbulent kinetic energy and Re_λ reduce to low values, causing the flow-field to lose its original intensity significantly, before a realistic flow-field occurs. The thermodynamic fluctuations, which have been initialised to zero, also take considerable time to approach realistic values, commensurate with the turbulent Mach number M_t of the flow-field. Moreover, the initial flow-field on account of being incompressible, cannot simulate higher turbulent mach numbers realistically. Thus, the flow-field resulting from this form of initialization is not entirely reflective of compressible isotropic turbulence.

The method of Erlebacher et. al. (1991) to generate an isotropic turbulent flow-field is described below.

3.2 Erlebacher et. al.'s method

Any general turbulent flow field can be decomposed into compressible and incompressible parts.

$$\mathbf{u} = \mathbf{u}^C + \mathbf{u}^I, \quad (3.12)$$

where the incompressible velocity satisfies the incompressible Navier Stokes mass and momentum conservation equations :

$$\begin{aligned}\nabla \cdot \mathbf{u}^I &= 0, \\ \frac{\partial \mathbf{u}^I}{\partial t} + \mathbf{u}^I \cdot \nabla \mathbf{u}^I &= -\nabla p^I,\end{aligned}\tag{3.13}$$

and the incompressible pressure p^I satisfies a Poisson equation

$$\nabla^2 p^I = -\nabla \mathbf{u}^I : \nabla \mathbf{u}^I.\tag{3.14}$$

This is used for formulating the initial flow field, which is given by

$$\mathbf{u}_0 = \mathbf{u}_0^C + \mathbf{u}_0^I,\tag{3.15}$$

where

$$\nabla \cdot \mathbf{u}_0^I = 0,\tag{3.16}$$

$$\nabla \times \mathbf{u}_0^C = 0,\tag{3.17}$$

by construction. The subscript 0 denotes the initial flow field. The decomposition is unique for homogeneous flows and is accomplished in Fourier space in the following manner

$$\hat{\mathbf{u}}^I = \hat{\mathbf{u}} - \frac{\mathbf{k} \cdot \hat{\mathbf{u}}}{k^2}.\tag{3.18}$$

A power four spectrum

$$E(k) = k^4 e^{-\left(\frac{k^2}{2k_0^2}\right)},\tag{3.19}$$

is imposed on each of the variables in the following manner with density ρ as the example. The wavenumber space is scanned and for each pair (k_x, k_y, k_z) , the corresponding spherical shell is determined. The i^{th} shell is defined by

$$\left(i - \frac{1}{2} < k < i + \frac{1}{2}\right), \quad (3.20)$$

where $k = \sqrt{k_x^2 + k_y^2 + k_z^2}$. The contribution of the i^{th} shell to the autocorrelation spectrum thus becomes

$$E_i^* = \sum_{i-\frac{1}{2} < k < i+\frac{1}{2}} |\hat{\rho}(\mathbf{k})|^2, \quad (3.21)$$

where E_i^* is the discrete representation of $\int_{i-\frac{1}{2}}^{i+\frac{1}{2}} E^*(k) dk$ and $\hat{\rho}$ is the discrete Fourier transform of ρ . Defining E^i as

$$E_i = E(i), \quad (3.22)$$

where $E(i)$ is obtained from equation for the power spectrum given above. Finally, the density is rescaled according to

$$\hat{\rho}(i) \leftarrow \hat{\rho}(i) \sqrt{\frac{E_i}{E_i^*}}, \quad (3.23)$$

to impose the desired spectrum. Thus, in a similar way, the autocorrelation spectra for \mathbf{u}^C , \mathbf{u}^I and T are calculated. It is important to note that the above procedure has to be performed separately for the three components of the velocity vector.

The quantities above are transformed back to physical space and can be rescaled to impose an appropriate root mean square value. For the velocity, there remains still a degree of freedom as \mathbf{u}^C and \mathbf{u}^I can be weighted independently without affecting the rms value of \mathbf{u} . This can be adjusted by defining the compressibility of the flow field as follows :

$$\chi = \frac{\int \mathbf{u}^{C^2} d\mathbf{x}}{(\int \mathbf{u}^{C^2} + \mathbf{u}^{I^2}) d\mathbf{x}}. \quad (3.24)$$

The denominator is the total kinetic energy of the system and the numerator is the total compressible kinetic energy associated with the system.

The mean non-dimensional values are added to the fluctuations obtained through the above procedure to obtain :

$$\rho \leftarrow 1 + \rho, \quad (3.25)$$

$$T \leftarrow 1 + T. \quad (3.26)$$

The pressure is obtained through the equation of state.

This form of initial conditions gives us the freedom of obtaining an initial flow field with arbitrary compressibility, turbulent mach number and rms values for the thermodynamic variables.

3.3 Ristorcelli and Blaisdell method

This method was developed by Ristorcelli and Blaisdell in 1997. Here it is shown that as a consequence of a nonzero turbulent mach number M_t , there are finite thermodynamic and dilatational fluctuations associated with the initial turbulent flow-field. The procedure to obtain this flow-field is described below.

Firstly, a small Mach number expansion of the compressible Navier-Stokes equations about the initial background quantities is constructed with the assumption that $M_t \ll 1$. Thus the velocity field is decomposed according to

$$u_i = v_i + \epsilon^2 w_i + \dots, \quad (3.27)$$

where $\epsilon^2 = \gamma M_t^2$, v_i are the solenoidal velocity fluctuations as per Rogallo (1981) and w_i are the compressible velocity fluctuations.

The thermodynamic variables are decomposed as the sum of a mean state and a perturbation about that mean state as follows:

$$p' = \bar{p}(1 + p), \quad (3.28)$$

$$T' = \bar{T}(1 + T), \quad (3.29)$$

$$\rho' = \bar{\rho}(1 + \rho). \quad (3.30)$$

The thermodynamic quantities with a prime are dimensional fluctuations and those with an overbar are dimensional mean values. The velocity fluctuations have been non-dimensionalized with their root mean square value. The perturbation series above can be expanded in the following form:

$$p = \epsilon^2(p_1 + \epsilon^2 p_2 + \dots), \quad (3.31)$$

$$T = \epsilon^2(T_1 + \epsilon^2 T_2 + \dots), \quad (3.32)$$

$$\rho = \epsilon^2(\rho_1 + \epsilon^2 \rho_2 + \dots), \quad (3.33)$$

where p_1 , T_1 and ρ_1 denote the first order fluctuations and p_2 , T_2 and ρ_2 denote second order fluctuations. Substituting these expressions in the governing equations, neglecting viscous terms and retaining only lowest order terms, we get the following equations

$$\frac{\partial v_i}{\partial x_i} = 0, \quad (3.34)$$

$$\frac{\partial^2 p_1}{\partial x_j \partial x_j} = -\frac{\partial^2 (v_i v_j)}{\partial x_i \partial x_j}, \quad (3.35)$$

$$\frac{\partial v_i}{\partial t} + v_p \frac{\partial v_i}{\partial x_p} + \frac{\partial p_1}{\partial x_i} = 0. \quad (3.36)$$

Equation 3.34 is a zeroth order measure of compressibility. In order to obtain a weakly compressible flow-field, a first order measure of compressibility is introduced as

$$\frac{\partial p_1}{\partial t} + v_k \frac{\partial p_1}{\partial x_k} = -\gamma d, \quad (3.37)$$

where d is the dilatation in the above equation which is the divergence of the com-

compressible velocity fluctuations w_i . Equation 3.35 is a Poisson equation for the pressure fluctuations which is solved first. Then, the time derivative of the pressure fluctuations is solved for which is also setup as a Poisson equation:

$$\frac{\partial^2}{\partial x_j \partial x_j} \left(\frac{\partial p_1}{\partial t} \right) = 2 \frac{\partial^2}{\partial x_i \partial x_j} \left[\left(v_k \frac{\partial v_i}{\partial x_k} + \frac{\partial p_1}{\partial x_i} \right) v_j \right]. \quad (3.38)$$

The pressure fluctuations and their temporal derivatives are now used to solve for the dilatation given by equation 3.37. The compressible velocity fluctuations are then obtained in Fourier space using

$$\hat{w}_j = -(k_j/k^2) \hat{d}. \quad (3.39)$$

The temperature and density fluctuations can be obtained from the pressure fluctuations and the linearized isentropic relations

$$\rho_1 = (1/\gamma) p_1, \quad (3.40)$$

$$T_1 = [(\gamma - 1)/\gamma] p_1. \quad (3.41)$$

Initialization Method	T	μ	p	Re	Re_λ
Rogallo (1981)	1	1	0.714	515	51.7
Erlebacher et. al. (1991)	1	1	0.714	515	42.5
Ristorcelli and Blaisdell (1997)	1	1	0.714	515	51.7

Table 3.1: Comparison of initial values of parameters for the simulations at 300K. All values have been non-dimensionalized with model 1 values at 300K.

3.4 Comparison of initial conditions

In this section, we compare the results from the initial conditions of Rogallo (1981), Erlebacher et.al. (1991) and Ristorcelli and Blaisdell (1997) by analysing the temporal evolution of turbulence statistics for low temperature weakly compressible isotropic turbulence. Table 3.1 shows the initial values of the parameters.

Figure 3.1 shows the the time evolution of various turbulent statistics for the different

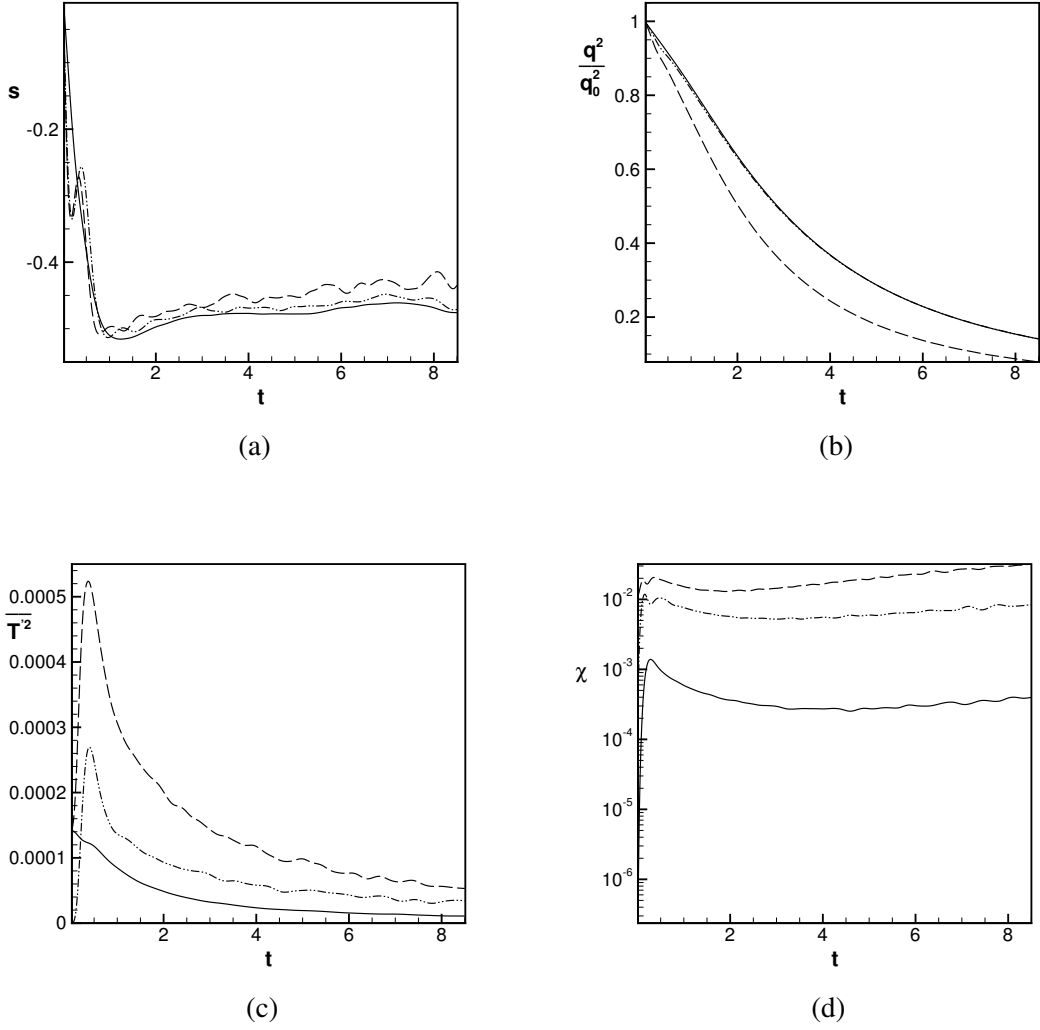


Figure 3.1: Comparison of turbulence statistics between three different isotropic turbulence initialization methods: (a) velocity derivative skewness s , (b) q^2/q_0^2 , (c) $\overline{T'^2}$ and (d) χ . — denotes Ristorcelli and Blaisdell (1997), ---- denotes Erlebacher et. al. (1991) and - · - · - denotes Rogallo (1981).

methods of initialization discussed in sections 3.1, 3.2 and 3.3. Figure 3.1a shows the time evolution of the velocity derivative skewness, given by

$$s = \frac{1}{3} (s_x + s_y + s_z) \quad (3.42)$$

where s_x , s_y and s_z are velocity derivative skewnesses along x , y and z coordinate directions respectively. s_x is given by

$$s_x = \frac{\overline{\left(\frac{\partial u}{\partial x}\right)^3}}{\left[\overline{\left(\frac{\partial u}{\partial x}\right)^2}\right]^{3/2}}. \quad (3.43)$$

s_y and s_z are obtained using similar expressions along y and z directions respectively. From figure 3.1a, it can be seen that skewnesses for all the simulations are in the range of -0.4 to -0.5 , which is consistent with results from literature (Touvalaris 1978). However, it is clear that the skewness from Rogallo (1981) and Erlebacher et. al. (1991) have oscillations in comparison to that of Ristorcelli and Blaisdell (1997) which is relatively flat. Figure 3.1b shows the time evolution of turbulent kinetic energy. All the forms of initialization, start from the same magnitude of turbulent kinetic energy (q^2). q^2 evolution rates are very similar for Rogallo (1981) and Ristorcelli and Blaisdell (1997). However, Erlebacher (1991) has a faster decay rate in comparison to the other two methods of initialization (figure 3.1b). This is consistent with previous results from Blaisdell (1991) and Samtaney et. al. (2001) who have shown that the asymptotic states of statistics in time evolution of decaying compressible isotropic turbulence is dependent on the initial conditions of the flow-field.

Figures 3.1c shows the time evolution of mean square temperature fluctuation, denoted by $\overline{T'^2}$. It can be seen that despite starting from the same initial value of 0.00015, there is a significant transience associated with the time evolution of $\overline{T'^2}$ for Rogallo (1981) and Erlebacher et. al. (1991). However for Ristorcelli and Blaisdell (1997), it can be seen that there is no transience. Similar behaviour is seen for compressibility χ , given by equation 3.24. The initialization by Erlebacher et. al. (1991) has significantly larger starting transience in comparison to Ristorcelli and Blaisdell (1997) (figure 3.1d).

For the initialization method by Rogallo (1981) the resulting velocity fluctuation flow-field is incompressible and there are no thermodynamic fluctuations. For the method by Erlebacher et. al. (1991), the velocity and thermodynamic fluctuations are independent and can be set arbitrarily. The compressibility can also be arbitrarily specified by altering the contributions of the compressible and incompressible parts of the velocity flow-field. Though this gives the freedom to set arbitrary initial conditions and study the effect of the turbulence evolution on different types of initial conditions, it is questionable whether the resulting flow-field is realistic or not. This is evident from the oscillations in the velocity derivative skewness and large transience observed for the mean square thermodynamic fluctuation and compressibility for both Rogallo (1981) and Erlebacher (1991). Ristorcelli and Blaisdell (1997), on the other hand has a flat velocity derivative skewness. There is no transience associated with the thermodynamic fluctuation quantities and minimal transience for the velocity divergence. Moreover, the

initial velocity fluctuation flow-field is strongly related to the pressure fluctuation flow-field through the dilatation. Consequently the thermodynamic fluctuations are coupled to the velocity fluctuations. In fact it has been shown in section 3.3 that for any non-zero M_t , finite thermodynamic fluctuations exist in the flow-field.

Considering these results, it has been decided that the method of Ristorcelli and Blaisdell (1997) will be used to simulate high temperature compressible decaying isotropic turbulence.

CHAPTER 4

Results and discussion

4.1 Flow-field initialization

As discussed in the previous chapter, three different methods of flow-field initialization have been implemented and tested. The method by Rogallo (1981) produces a divergence free flow-field with no fluctuation in the thermodynamic fields. The method by Erlebacher et. al. (1990) splits the velocity field into incompressible and compressible components and uses a power four spectrum for the velocity and thermodynamic fields. The method by Ristorcelli and Blaisdell (1997) produces a weakly compressible flow-field, given an incompressible fluctuating velocity field. The method also proves that for any non-zero M_t , finite thermodynamic fluctuations exist, along with the weakly compressible flow-field. Amongst the three methods, the initialization procedure by Ristorcelli and Blaisdell (1996) has been chosen as the most appropriate one as in this case one can start with an initial flow-field which has an accurate estimate for the fluctuations in the velocities as well as in the thermodynamic quantities.

4.2 Low temperature simulation

Simulations of decaying isotropic turbulence are carried out for models 1 and 2 at an initial mean temperature of 300K. Initial Re_λ and initial mean temperature T_0 are chosen to be the same for both the models. The initial energy spectrum used for the incompressible velocity is a power four spectrum. This simulation uses a resolution of $256 \times 256 \times 256$ grid points in x, y and z directions. Figure 4.1a shows the normalized turbulent kinetic energy evolution in time and figure 4.1b shows the time evolution of vorticity, with an initial value of 13.2. The good agreement between results obtained from models 1 and 2 is to be expected as at these temperatures model 2 should fall back upon model 1. This further serves as additional validation that the implementation of the solver and physical models are correct.

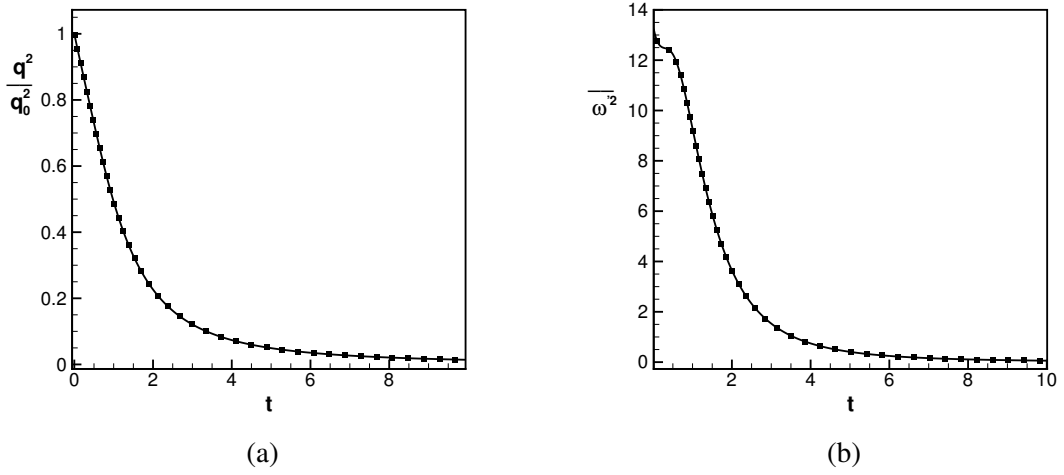


Figure 4.1: Comparison of (a) turbulent kinetic energy and (b) vorticity between models 1 and 2 at 300K. — denotes model 1 and ■ denotes model 2

Model	T	μ	p	R	Re_λ
1	50	13.75	0.191	0.714	33.146
2b	50	4.83	0.191	0.714	113.066

Table 4.1: Comparison of initial values of flow parameters for simulations at 15000K for models 1 and 2b. All values have been non-dimensionalized suitably with Model 1 values at 300K with the exception of Re_λ .

4.3 High temperature simulation

The initial conditions are as described in the previous section. The computational Reynolds number Re is fixed across all model simulations at the value of 100000. The initial energy spectrum used for the incompressible velocity is a power four spectrum. All simulations are at an initial background mean temperature of 15000K.

4.3.1 Comparison between models 1 and 2b

This section highlights the impact of model 2 based transport properties on the flow-field. Table 4.1 shows initial values for the flow parameters used for models 1 and 2b at 15000K. These values are non-dimensionalised with model 1 values of the corresponding flow parameters at 300K. Recall that model 1 uses perfect gas model for both the thermodynamic and transport properties while model 2b uses perfect gas based thermodynamic properties and L.T.E. based transport properties. Figure 4.2a shows the time

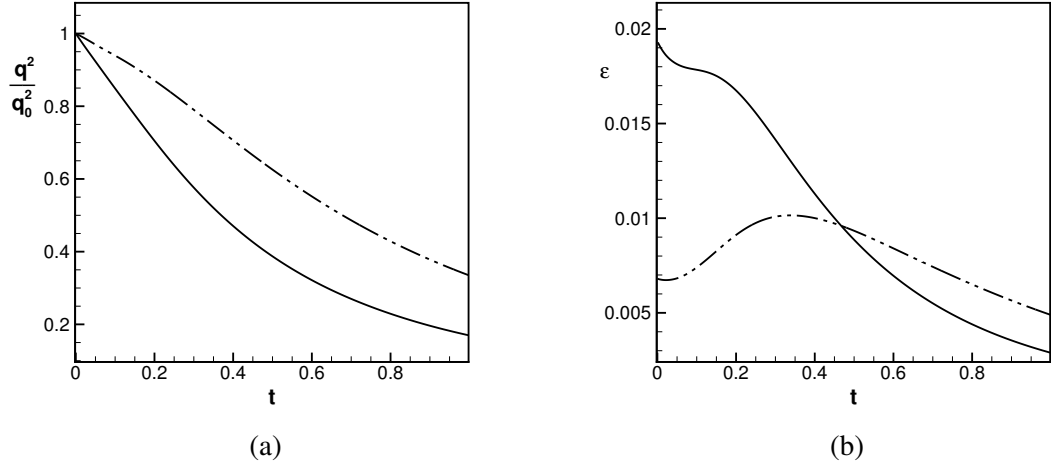


Figure 4.2: Comparison of (a) q^2/q_0^2 and (b) ϵ between models 1 and 2b at 15000 K. — represents model 1 and - · - · - represents model 2b.

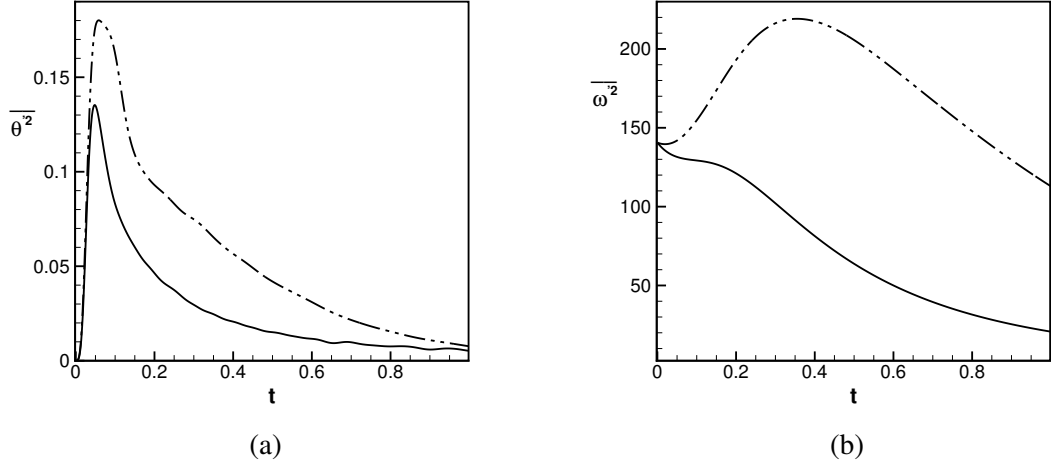


Figure 4.3: Comparison of (a) $\overline{\theta'^2}$ and (b) $\overline{\omega'^2}$ between models 1 and 2b at 15000K. — represents model 1 and - · - · - represents model 2b.

evolution of turbulent kinetic energy q^2 for Models 1 and 2b. q^2 decays at a faster rate for model 1 in comparison to model 2b. This can be attributed to dissipation ϵ for the models shown in figure 4.2b. A look at the turbulent kinetic energy budgets shows that only dissipation plays an important role in the time evolution of q^2 . ϵ is observed to be higher for model 1 initially, but decreases and later becomes lower than that for model 2b. In general, ϵ for compressible isotropic turbulence (Blaisdell 1990) is given by

$$\epsilon = \underbrace{\frac{\bar{\mu}}{Re} \overline{\omega'_i \omega'_i}}_{\text{solenoidal dissipation}} + \frac{4}{3} \underbrace{\frac{\bar{\mu}}{Re} \frac{\partial u'_i}{\partial x_i} \frac{\partial u'_j}{\partial x_j}}_{\text{dilatational dissipation}} \quad (4.1)$$

The first term denotes the solenoidal/vortical component of dissipation while the second term denotes the dilatational component. The contribution from the dilatational part is small and the vortical part dominates (figures 4.3a and 4.3b). So, dissipation can simply be given by

$$\epsilon = \frac{\bar{\mu}}{Re} \overline{\omega'_i \omega'_i} \quad (4.2)$$

It may be noted that the coefficient of viscosity $\bar{\mu}$ in equation 4.2 remains almost three times higher for model 1 when compared to model 2b. So, if this were the only quantity determining dissipation, dissipation for model 1 would remain about three times higher than that for model 2b at all times. However, dissipation is also affected by enstrophy. Hence, to understand the nature for time evolution of dissipation for the two models, one needs to understand time evolution of enstrophy. Budgets were computed for the enstrophy transport equation

$$\begin{aligned} \frac{\partial}{\partial t} (\overline{\omega'_i \omega'_i}) = & \underbrace{\overline{\omega'_i \omega'_j \left(\frac{\partial u''_i}{\partial x_j} + \frac{\partial u''_j}{\partial x_i} \right)}}_{\text{vortex stretching}} - \underbrace{\overline{\omega'_i \omega'_i \frac{\partial u''_j}{\partial x_j}}}_{\text{enstrophy-dilatation}} + \underbrace{\overline{2\omega'_l \epsilon_{lki} \frac{1}{\rho^2} \frac{\partial \rho}{\partial x_k} \frac{\partial p}{\partial x_i}}}_{\text{baroclinic}} + \\ & \underbrace{\frac{2}{Re} \epsilon_{ikl} \overline{\frac{\partial \omega'_l}{\partial x_k} \frac{1}{\rho} \frac{\partial}{\partial x_j} \left[\mu \left(\frac{\partial u''_i}{\partial x_j} + \frac{\partial u''_i}{\partial x_i} - \frac{2}{3} \frac{\partial u''_m}{\partial x_m} \right) \right]}}_{\text{vortex dissipation}}. \end{aligned} \quad (4.3)$$

Vortex stretching and viscous dissipation were the only terms that were found to play a dominant role. Figure 4.4a shows time evolution of the vortex stretching term. It is found to increase initially with time and reach a peak, beyond which it is found to decrease. Also, magnitude of vortex stretching is much greater for model 2b, when compared to model 1. Figure 4.4b shows time evolution of viscous dissipation term for Models 1 and 2b. Viscous dissipation is found to be negative in magnitude. Initially, it decreases until it attains a maximum negative value, and then increases again. Also, it is more significant for model 2b. Enstrophy-dilatation interaction term is also shown in figure 4.4c. Magnitudes of time variation of this term is found to be insignificant when compared to vortex stretching and viscous dissipation terms. Figure 4.4d shows time evolution of the sum of all the terms on the right-hand side of the enstrophy transport

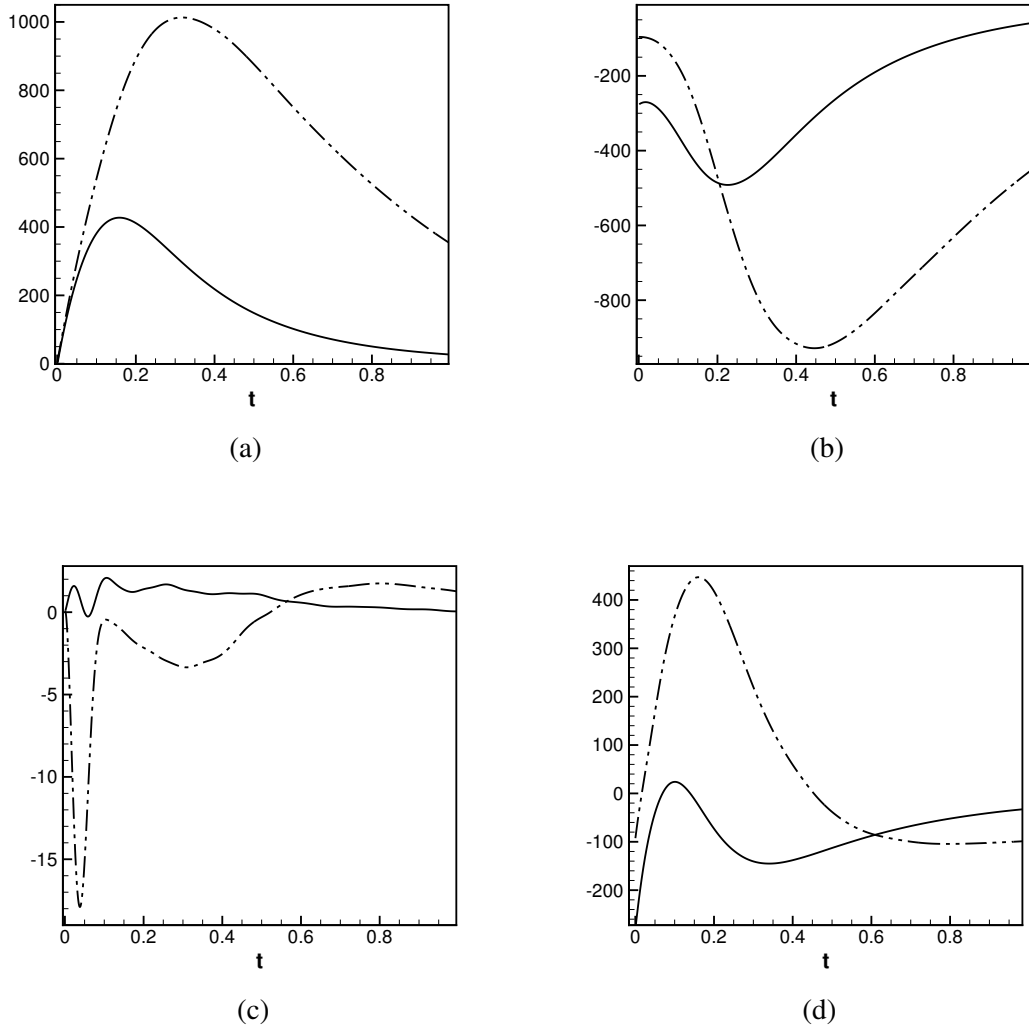


Figure 4.4: Enstrophy budgets: Comparison of (a) vortex stretching, (b) vortex dissipation, (c) enstrophy-dilatation interaction and (d) total right hand side of enstrophy transport equation between models 1 and 2b at 15000 K. — represents model 1 and - - - - represents model 2b.

equation. Again, the values are found to be much more for model 2b when compared to model 1. Thus, more enstrophy is produced for model 2b as compared to model 1. Going back to equation 4.2, recall that dissipation depends on both the absolute magnitude of the viscosity coefficient $\bar{\mu}$ and the enstrophy produced. While $\bar{\mu}$ for model 1 is three times that for model 2b, enstrophy production is always more for model 2b. Hence initially, dissipation is more for model 1. However, the difference between the two models decreases with time and after some time, dissipation is larger for model 2b. This is reflected in the time evolution for turbulent kinetic energy (figure 4.2a). As initially, dissipation is more for model 1, decay of turbulent kinetic energy is more. This decay rate slows down over time for model 1. For model 2b, decay rate increases over time with ϵ as observed in figure 4.2b. Thus, the curve does not flatten as observed for

q^2 evolution for model 2b (figure 4.2a).

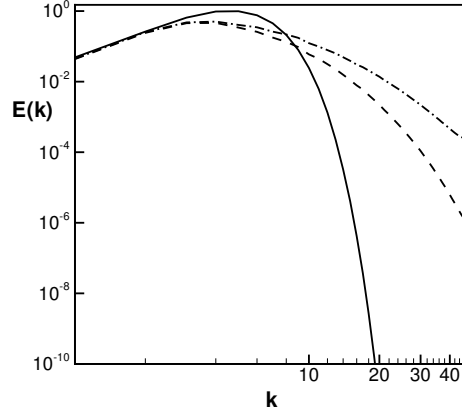


Figure 4.5: Comparison of energy spectra between models 1 and 2b at 15000K. — denotes the initial spectrum, ---- denotes the spectrum of model 1 and -.-.-.- denotes the spectrum of model 2b at $t = 0.5$.

Figure 4.5 shows the energy spectra for both Models 1 and 2b at $t = 0.5$. Model 2b is shown to cover a wider range of length scales in comparison to model 1. This is because of larger vortex stretching in case of model 2b. Also, the magnitude of energy in the smaller length scales is higher for model 2b when compared to model 1. This shows that more energy has decayed from the larger length scales to the smaller length scales for model 2b than for model 1. Recall that both the models have been initialized to have the same magnitude and distribution of turbulent kinetic energy initially.

Putting all this together, one can conclude that the effect of L.T.E based transport properties is to enhance enstrophy levels in the flow resulting in higher dissipation and hence leading to increased decay of turbulent kinetic energy.

Figures 4.6a and 4.6b show the temporal variation of mean temperature and internal energy for both the models. For both Models 1 and 2b, the internal energy has a linear temperature dependence. For model 2, on the other hand, the internal energy has a non-linear dependence on temperature, given by figure 2.1a. The increase in temperature can be attributed to the decay of q^2 . The energy stored in the solenoidal and dilatational modes of q^2 , decay into the internal energy over time, causing a rise in the temperature of the flow-field. As the eddy turn over time of model 2b is larger than model 1, it takes time for the turbulence to decay for model 2b. As a result, it takes longer for the asymptotic equilibrium temperature to be reached, in comparison to model 1.

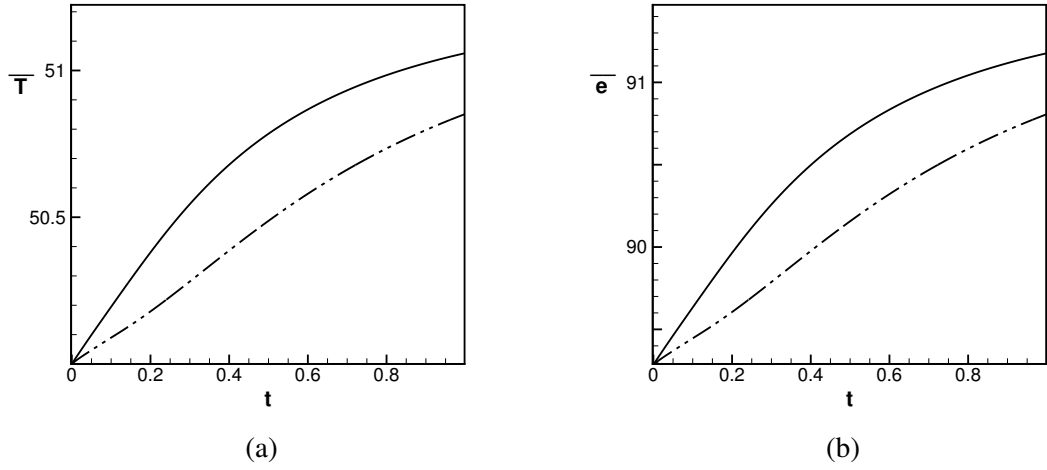


Figure 4.6: Comparison of (a) \bar{T} and (b) \bar{e} between models 1 and 2b at 15000 K. — represents model 1 and - · - · - represents model 2b.

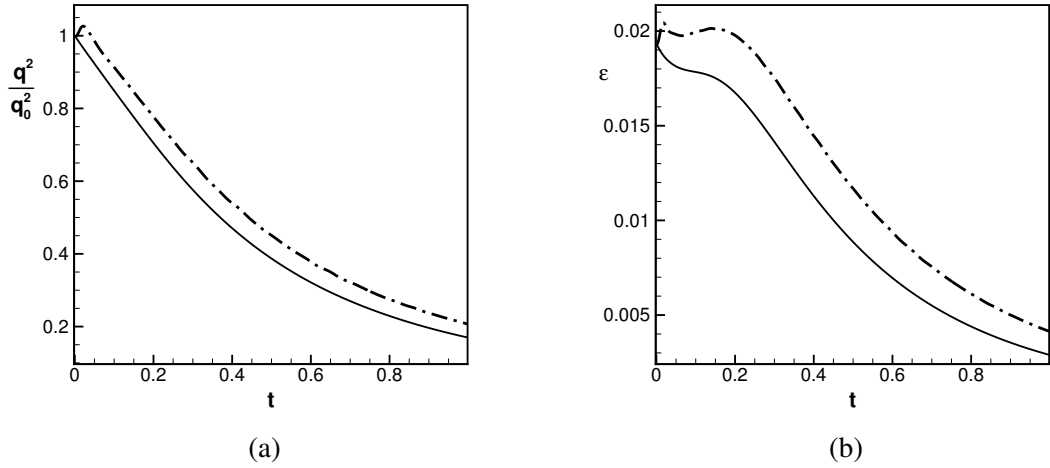


Figure 4.7: Comparison of (a) q^2/q_0^2 and (b) ϵ between models 1 and 2a at 15000 K. — represents model 1 and - · - · - represents model 2a.

4.3.2 Comparison between models 1 and 2a

This section highlights the impact of L.T.E. based thermodynamic properties. Table 4.2 shows the initial values for flow parameters for models 1 and 2a at 15000K. These values are non-dimensionalised with model 1 values of the corresponding flow parameters at 300K.

Figure 4.7a shows the time evolution of turbulent kinetic energy for models 1 and 2a. Model 2a has higher dissipation than model 1 as shown in in figure 4.7b. Unlike section 4.3.1, the dissipation for both the models starts from the same value as magnitudes of the initial viscosity and enstrophy are the same in both cases. Recall that dissipation is

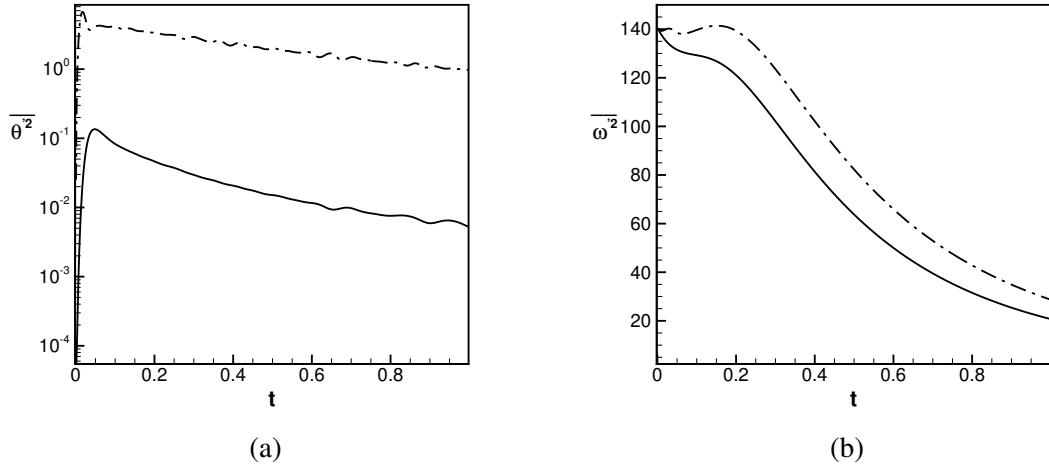


Figure 4.8: Comparison of (a) $\overline{\theta'^2}$ and (d) $\overline{\omega'^2}$ between models 1 and 2a at 15000K. — represents model 1 and - - - - represents model 2a.

Model	T	μ	p	R	Re_λ
1	50	13.75	0.191	0.714	33.146
2a	50	13.75	0.746	2.186	39.775

Table 4.2: Comparison of initial values of flow parameters for simulations at 15000K for models 1 and 2a. All values have been non-dimensionalized suitably with Model 1 values at 300K, with the exception of Re_λ .

composed of dilatational and vortical parts (equation 4.1). Figure 4.8 shows the time evolution of dilatation and enstrophy for Models 1 and 2a. It is interesting to note that the dilatation for model 2a is larger than that of model 1 by over an order of magnitude as shown in figure 4.8a. However, the vorticity magnitude from figure 4.8b is significantly larger than the divergence. Hence, equation 4.2 gives a good approximation for the total dissipation for model 2a as well.

In order to better understand the variation of enstrophy with time, budgets were computed for the right-hand side of the enstrophy transfer equation. Vortex stretching, viscous dissipation and enstrophy-dilatation terms are found to be significant in this case. Vortex stretching (figure 4.9a) is found to be higher for model 2a in comparison to model 1. Similarly, there is more vorticity dissipation (figure 4.9b) associated with the flow-field for model 2a than for model 1. The enstrophy-dilatation interaction term also plays a role in the initial stages of the time-evolution of the flow-field, as shown in figure 4.9c. However, its effects are temporary. Figure 4.9d shows the sum of all the terms on the right-hand side of equation 4.3. The appearance of the first peak can be

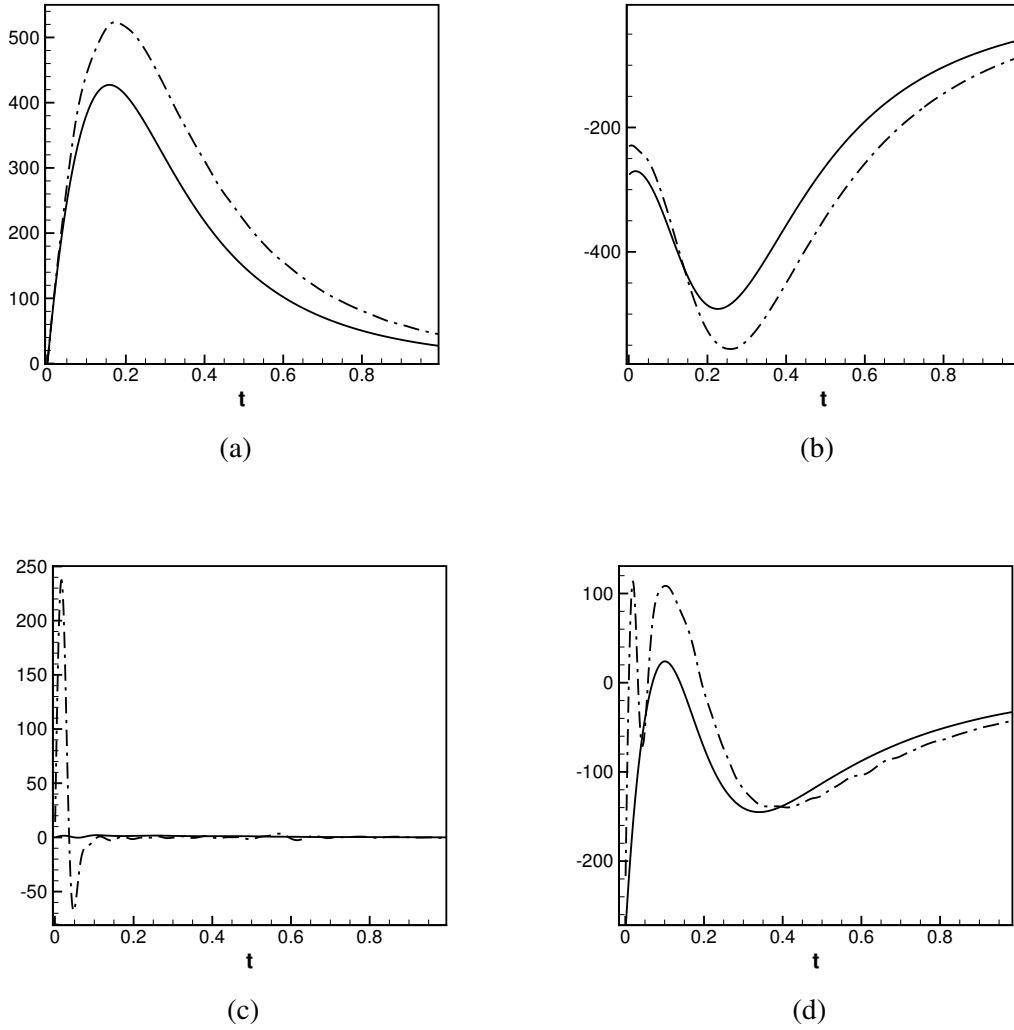


Figure 4.9: Enstrophy budgets: Comparison of (a) vortex stretching, (b) vortex dissipation, (c) enstrophy-dilatation interaction and (d) total rate of enstrophy evolution between models 1 and 2a at 15000 K. — represents model 1 and - - - - represents model 2a.

attributed to the transient enstrophy-dilatation interaction, while the second peak can be attributed to the net production of enstrophy by vortex stretching. The effect of the transient enstrophy- dilatation interaction can also be seen in the evolution of q^2 for model 2a in figure 4.7a, where there is an initial increase in the turbulent kinetic energy.

It is interesting to note that in comparison to models 1 and 2b, there is a smaller difference in the dissipation of models 1 and 2a. This can be attributed to the fact that both these models follow the same power law temperature dependence for viscosity. From this, it is possible to conclude that the transport properties play a significant role in the time evolution of enstrophy. Therefore, the transport properties dominate the dissipation characteristics of the isotropic turbulent flow-field through the enstrophy.

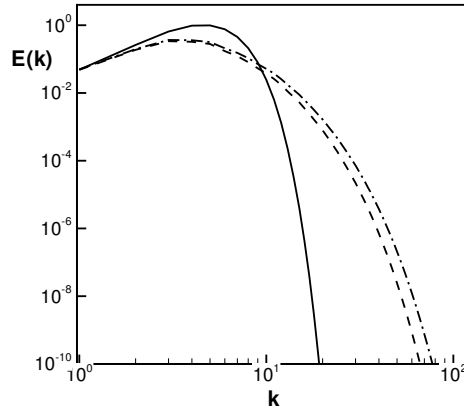


Figure 4.10: Comparison of energy spectra between models 1 and 2a at 15000K. — denotes the initial spectrum, - - - - denotes the spectrum of model 1 and the - . - . - . denotes the spectrum of model 2a at $t = 0.5$.

Figure 4.10 shows the energy spectra of models 1 and 2a at $t = 0.5$. The energy distribution at the smaller length scales for model 1 is only marginally different from that for model 2a. This is in contrast to the energy spectra for models 1 and 2b (figure 4.5).

The dilatation, on the other hand is influenced by the thermodynamic properties. This can be observed by comparing figures 4.3a and 4.8a.

Figure 4.11 show the temporal evolution of internal energy. It is interesting to note that the internal energy for model 2a is about 10 times that of model 1 at all times. This is due to the non-linear dependence of internal energy on temperature for model 2a, in contrast to the linear temperature dependence for model 1. Thus, the amount of internal energy that is associated with the flow-field is very different. The total asymptotic increase in the internal energy is equal to the initial value of q^2 because both the models were initialized with the same amount of turbulent kinetic energy.

4.3.3 Comparison between models 1 and 2

In this section, the cumulative effect of the thermodynamic and transport properties on the flow-field will be discussed. Table 4.3 shows initial values for flow parameters for models 1 and 2 at 15000K. These values are non-dimensionalised with model 1 values of the corresponding flow parameters at 300K.

Figures 4.12a and 4.12b show q^2 and ϵ for models 1 and 2 respectively. It can be ob-

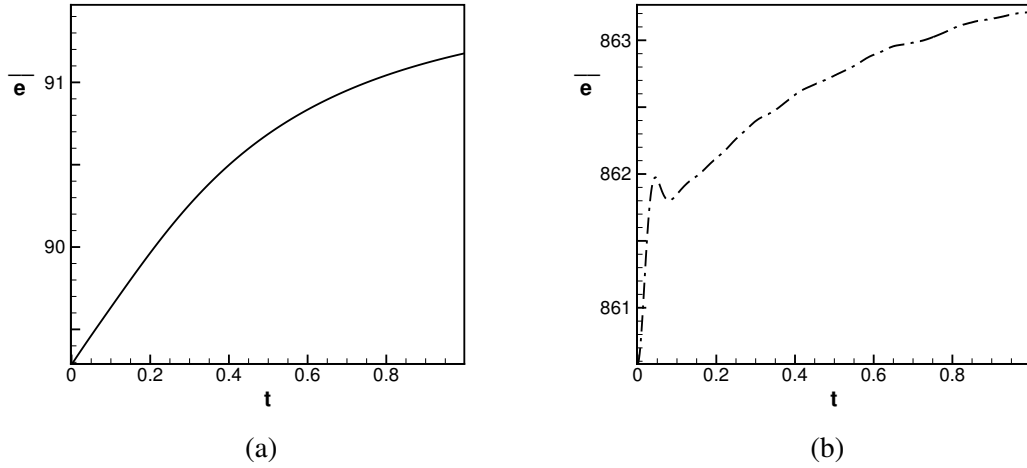


Figure 4.11: Comparison of (a) \bar{e} for model 1 and (b) \bar{e} for model 2a at 15000K. — represents model 1 and - - - - represents model 2a.

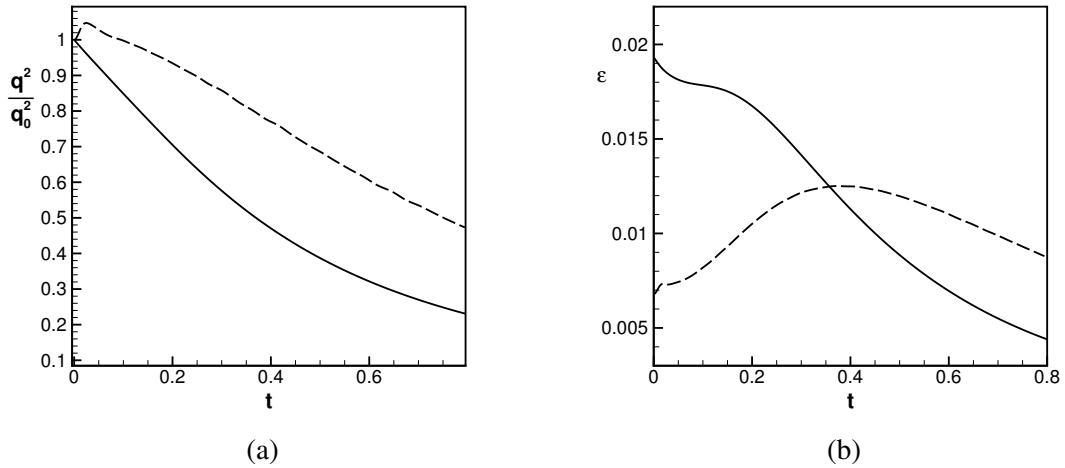


Figure 4.12: Comparison of (a) q^2/q_0^2 and (b) ϵ between models 1 and 2 at 15000 K. — represents model 1 and - - - - represents model 2.

served that the dissipation characteristics of model 2 are very similar to that of model 2b (figures 4.12b and 4.2b respectively). The initial decay of q^2 is faster for model 1 in comparison to model 2. However an increase in the enstrophy due to strong vortex stretching and subsequently high solenoidal dissipation is responsible for model 2 having a higher dissipation rate later in time. The initial increase in turbulent kinetic energy, observed due to the transient effects of enstrophy-dilatation interaction in model 2a is also visible for model 2 (figure 4.14c).

Figure 4.13a shows the time evolution of dilatation of models 1 and 2. Model 2 has dilatation that is higher by more than an order of magnitude in comparison to model 1. This is an effect of the L.T.E. based thermodynamic properties and was also seen

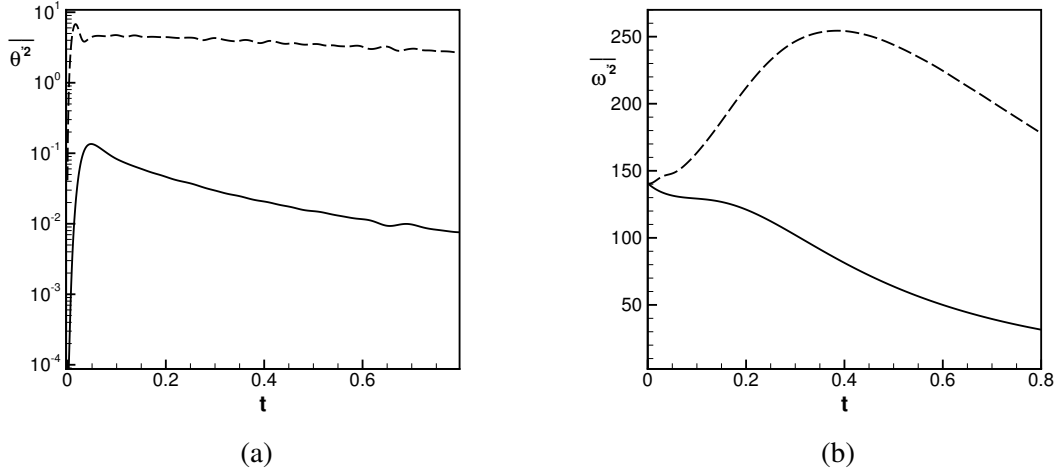


Figure 4.13: Comparison of (a) $\overline{\theta'^2}$ and (b) $\overline{\omega'^2}$ between models 1 and 2 at 15000K. — represents model 1 and - - - - represents model 2.

Model	T	μ	ρ	R	Re_λ
1	50	13.75	0.191	0.714	33.146
2	50	4.83	0.746	2.186	113.066

Table 4.3: Comparison of initial values of flow parameters for simulations at 15000K for models 1 and 2. All values have been non-dimensionalized suitably with Model 1 values at 300K, with the exception of Re_λ .

in section 4.3.2 for model 2a. On the other hand, the enstrophy evolution process for model 2 shown in figure 4.13b is similar to model 2b. Budget of the terms on the right-hand side of the enstrophy evolution equation reveal that the separate effects of transport and thermodynamic properties as described in previous sections are strongly visible in the temporal evolution of the turbulent statistics for model 2. Similar to what was observed in section 4.3.1, there are strong vortex stretching and vortex dissipation effects (figures 4.14a and 4.14b). Apart from these two factors, the enstrophy-dilatation interaction, represented by figure 4.14c also plays a role in the initial stages. Recall that a similar effect was observed for model 2a.

The energy spectrum (figure 4.15) further shows the energy content in the various length scales for both models 1 and 2 at $t = 0.5$. Note that the turbulent kinetic energy in model 2 is distributed across a wider range of length scales in comparison to model 1. Also, across the larger wavenumbers, model 2 has more energy per wavenumber than model 1. This is indicative of a stronger vortex stretching mechanism that has caused the distribution of energy from the large length scales to smaller length scales.

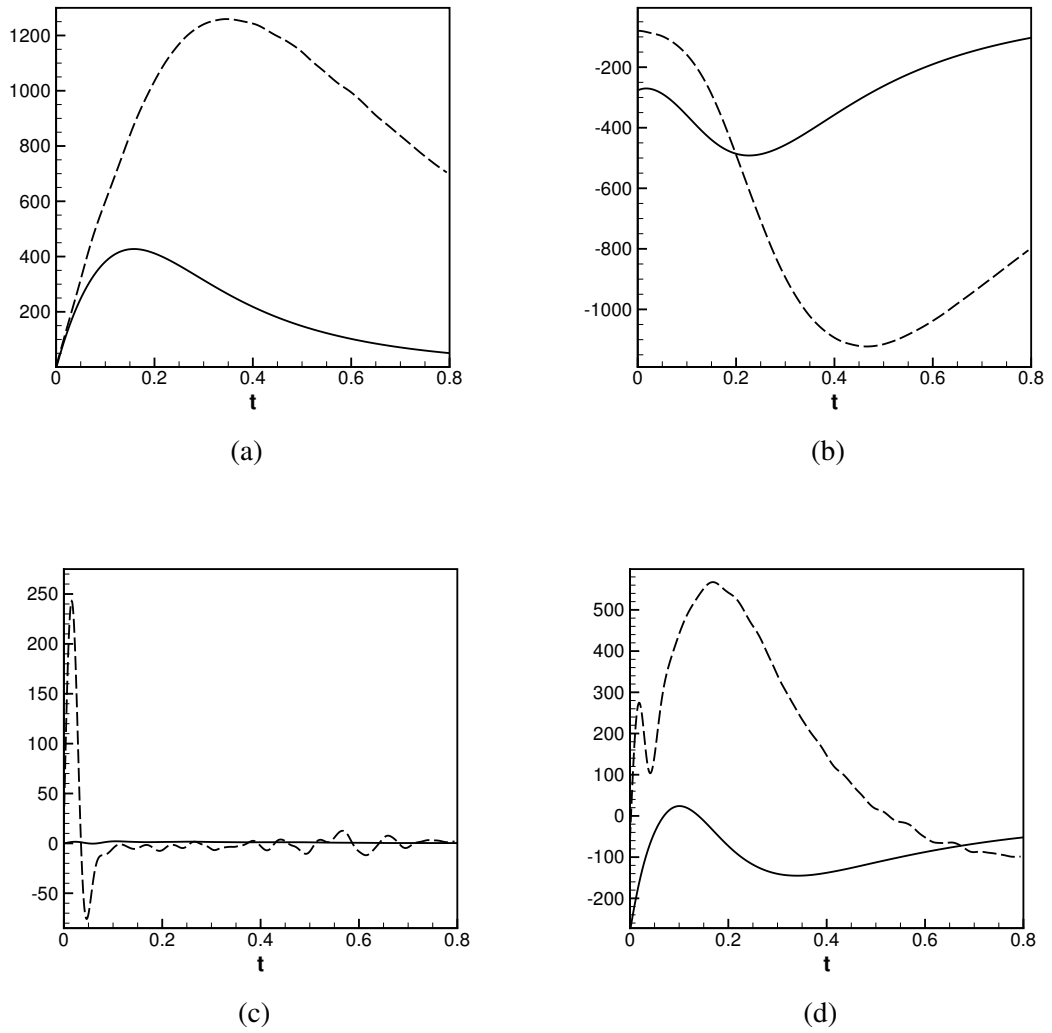


Figure 4.14: Enstrophy budgets: Comparison of (a) vortex stretching, (b) vortex dissipation, (c) enstrophy-dilatation interaction and (d) total rate of enstrophy evolution between models 1 and 2 at 15000 K. — represents model 1 and - - - - represents model 2.

As expected, the spectral behaviour for model 2 is closer to model 2b when compared to model 2a.

Figure 4.16 shows the time evolution of the mean internal energy for Models 1 and 2. It may be observed that the energy content for model 2 is much larger than that of model 1 because the thermodynamic properties for model 2 are computed using the high temperature L.T.E. based model.

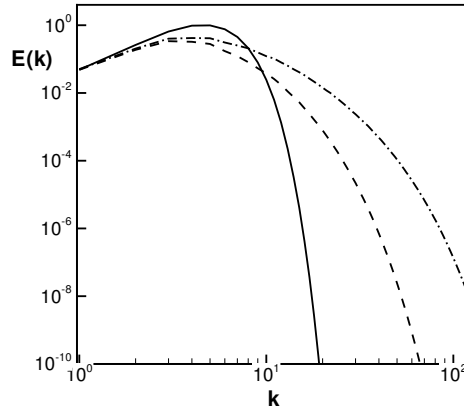


Figure 4.15: Comparison of energy spectra between models 1 and 2 at 15000K. — denotes the initial spectrum, — — — — denotes the spectrum of model 1 and - . - . - . denotes the spectrum of model 2 at $t = 0.5$.

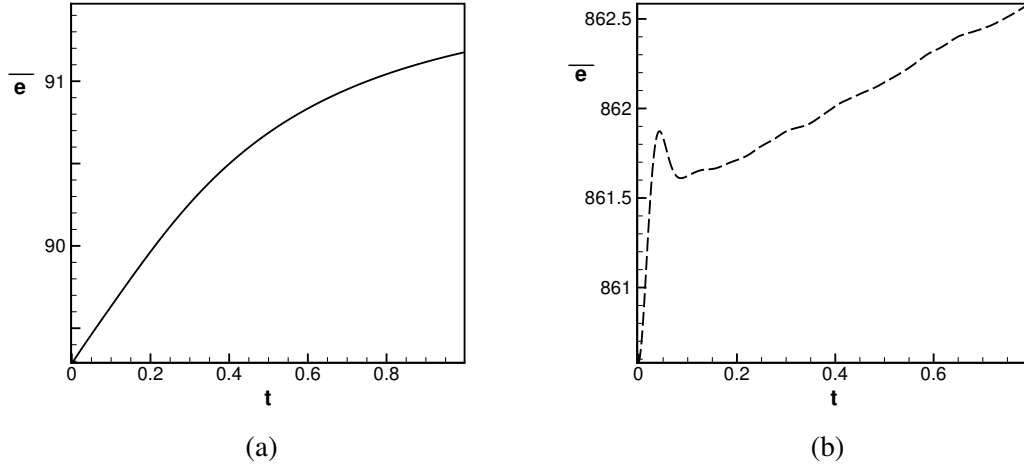


Figure 4.16: Comparison of (a) \bar{e} for model 1 and (b) \bar{e} for model 2 at 15000K. — represents model 1 and — — — — represents model 2.

4.4 Length scales for isotropic turbulence at high temperatures

The range of length scales in an isotropic turbulent flow-field can be represented by the ratio λ/η where λ denotes the Taylor microscale and η denotes the Kolmogorov scale. They are given by

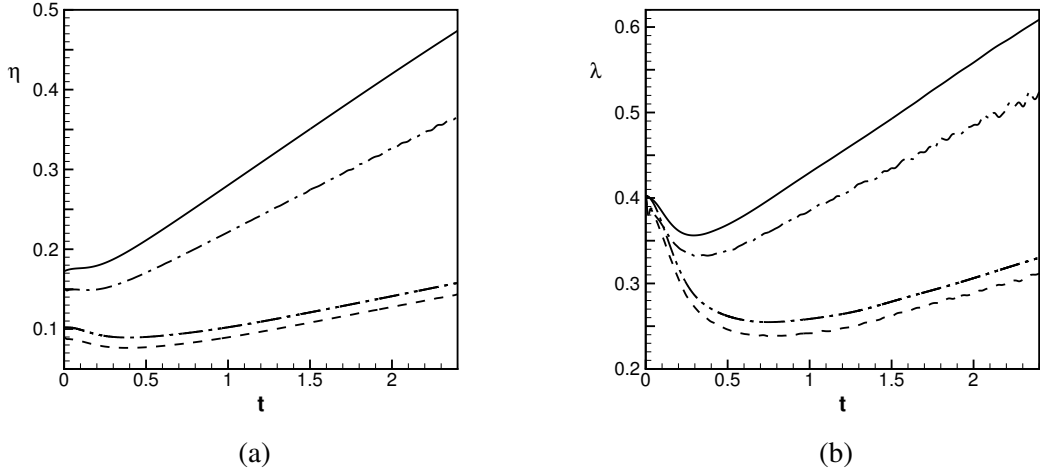


Figure 4.17: Comparison of (a) η and (b) λ for all models at 15000K. — represents model 1 and - - - - represents model 2.

$$\eta = \left(\frac{(\nu/Re)^3}{\epsilon} \right)^{(1/4)}, \quad (4.4)$$

$$\lambda = \sqrt{\frac{\overline{u'^2}}{\left(\frac{\partial u'}{\partial x} \right)^2}},$$

where ν denotes the kinematic viscosity. λ is representative of the average turbulence length scale while η is representative of the dissipation length scale. Figures 4.17a and 4.17b show the time evolution of η and λ respectively for all models. Both the length scales can be seen to decrease slightly first and then increase with a constant slope. It is also interesting to note that the range of values for λ is at least twice as large as that of η initially. This is to be expected as the turbulence length scales are generally larger than the dissipation length scales.

Figure 4.18a shows the ratio of λ/η across all models. The ratio λ/η represents the range of length scales in the flow-field. Larger the range of length scales, stronger the process of cascading from the turbulence length scales to the dissipative length scales. This ratio decreases with time consistently for all models. In order to understand this behaviour, figure 4.18b shows the normalized plots of λ and η . They have been normalized with their initial values respectively. This makes it convenient to compare the slopes of the curves. Figure 4.18b clearly shows that the rate of increase of η is higher than that of λ . This is qualitatively consistent with the fact that over time, as the cascading-

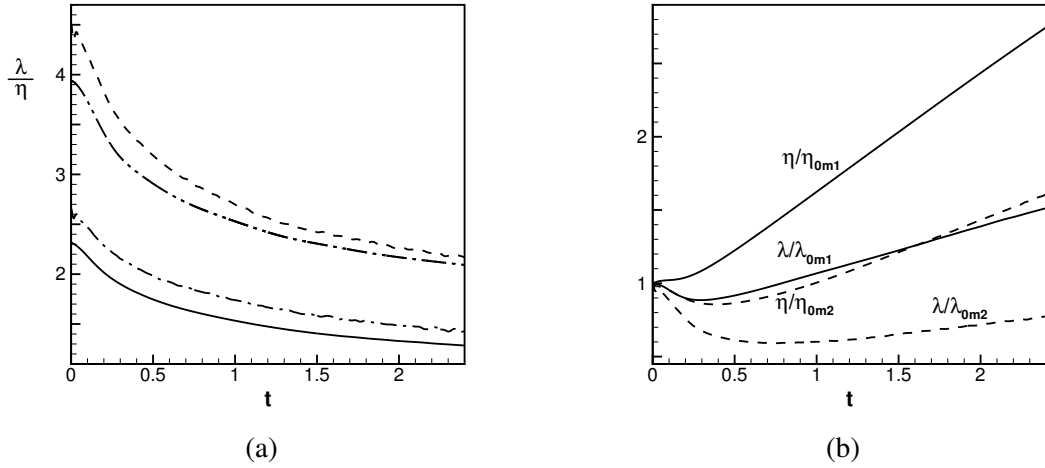


Figure 4.18: Comparison of (a) λ/η for all models and (b) λ/λ_0 , η/η_0 for models 1 and 2 at 15000K. For (a), — represents model 1, - - - - represents model 2a, - · - · - represents model 2b and - - - - - represents model 2.

ing of eddies occur from the turbulence length scales to the dissipation length scales, there is lesser contribution from the turbulence length scales to the overall turbulent kinetic energy. As most of the eddies have been re-distributed to the dissipation length scales, there is significant activity in the dissipation length scales which causes it to increase faster than λ . Consequently, we see that the ratio λ/η decreases with time (figure 4.18a). It is also important to note that this ratio is the largest for model 2, followed by 2b, then 2a and finally 1. This is consistent with fact that the enstrophy magnitudes also follow the same order. Thus, it can be reasoned that significant vorticity effects noticed for models 2 and 2b in comparison to models 1 and 2a are due to the presence of a larger range of length scales which facilitate enhanced vortex stretching and dissipation for the former in comparison to the latter.

CHAPTER 5

Summary

High temperature effects on decaying compressible isotropic turbulence are studied. L.T.E. conditions are assumed to apply as the time-scales associated with equilibration of chemical reactions are typically much smaller when compared to the turbulence time-scales. Four different physical models for air have been proposed. Model 1 assumes air to be a calorically and thermally perfect gas. Constant specific heats are assumed. The transport properties are monotonic functions of temperature. This kind of model has been used to study isotropic turbulence in past literature and hence serves as a base case for comparison with other high temperature based models. Model 2 accounts for the fact that as temperature is increased air molecules undergo vibrational excitation and chemical reactions. Both the thermodynamic and transport properties become functions of temperature. Specific heats are no longer constant. As the coefficient of viscosity is found to decrease sharply beyond 10000K, it may affect the decay of compressible isotropic turbulence all by itself. Thus, to decouple the effects of thermodynamic and transport properties on compressible isotropic turbulence and study them separately, model 2 is subdivided into models 2a and 2b. For model 2a, thermodynamic properties are obtained using L.T.E. based high temperature model while transport properties are computed as per model 1. For model 2b on the other hand, thermodynamic properties are computed based on model 1 and transport properties are obtained using the L.T.E based high temperature model.

Compressible isotropic turbulence is characterised by a wide range of length and time scales. A fully parallel, Fourier based pseudo-spectral Navier-Stokes flow solver is developed for simulating compressible isotropic turbulence. Spectral methods offer exponential convergence and are thus desirable to study turbulence. De-aliasing of the derivatives of non-linear terms is performed by using a skew-symmetric representation. Oddball wave number filtering is performed to prevent energy accumulation in the highest wavenumbers. A fourth order explicit Runge-Kutta scheme is used for time advancement. The flow solver is fully parallelized using MPI and validated using benchmark problems. The simulation domain is a cube of non-dimensional size 2π along

each of the x, y and z directions. Periodic boundary conditions are used along all directions. Three different methods to generate an isotropic turbulent flow-field are tested. The method by Ristorcelli and Blaisdell (1997) is found to be the most appropriate for high temperature simulations of compressible isotropic turbulence with a flat velocity derivative skewness and minimal transience associated with the velocity divergence and thermodynamic fluctuations.

At low temperatures, the L.T.E. based models should fall back upon model 1 as at these temperatures, none of the high temperature effects are observed. This is demonstrated by simulating decaying compressible isotropic turbulence using models 1 and 2 at 300K. Turbulent statistics are computed using volumetric averages.

Next, high temperature simulations of decaying compressible isotropic turbulence are performed at an initial mean temperature of 15000K. The computational Reynolds number Re and initial turbulent kinetic energy q_0^2 are fixed across all models. Comparison of models 1 and 2b highlight the effects of L.T.E. based transport properties at high temperatures. Turbulent kinetic energy is found to decay faster for model 1 than for model 2b initially. However after some time, the decay is stronger for model 2b. This can be explained based on time evolution of dissipation. The turbulent kinetic energy budget reveals turbulent dissipation to be the only non-negligible term. It is mainly comprised of solenoidal/vortical and dilatational components. Solenoidal dissipation is orders of magnitude stronger than dilatational dissipation for both models. The enstrophy budget shows competing effects of vortex stretching and vortex dissipation that affect the magnitude of enstrophy in the flow-field. Vortex stretching leads to enstrophy production while the dissipation term leads to a decrease in enstrophy. These effects are stronger for model 2b when compared to model 1. This combined with the values of $\bar{\mu}$ for the two models explains the time evolution behaviour of q^2 . The energy spectra for both the models show larger dispersion of energy across the smaller length scales for model 2b in comparison to model 1. This is consistent with higher vortex stretching observed for model 2b.

Comparison of models 1 and 2a highlight the effects of L.T.E based thermodynamic properties at high temperatures. Turbulent kinetic energy is found to decay faster for model 2a than for model 1. Thermodynamic properties have a direct effect on flow dilatation. The dilatation is found to be an order of magnitude stronger for model 2a than

model 1. The turbulent kinetic energy budget reveals turbulent dissipation to be the only non-negligible term. Again, solenoidal dissipation is found to be much stronger than dilatational dissipation for both models. To understand the time evolution of vorticity field, enstrophy budget was computed and vortex stretching, viscous dissipation and enstrophy-dilatation interaction terms were found to be predominant. The enstrophy-dilatation term soon becomes negligible. Net effect of the vortex stretching and the dissipation terms gives us the rate of enstrophy production. This coupled with the fact that $\bar{\mu}$ remains more or less the same for both the models gives us the q^2 decay behaviour observed in this case. The energy spectra for both the models show larger dispersion of energy across the smaller length scales for model 2a in comparison to model 1. This is consistent with higher vortex stretching observed for model 2a. However, the difference in dissipation between models 1 and 2a are not as large as those seen between models 1 and 2b. This effect is reflected in the energy spectra as well and more energy per unit wavenumber is observed in the smaller length scales for model 2b when compared to model 2a.

Comparison of models 1 and 2 highlight the cumulative effects of both L.T.E based thermodynamic and transport properties. Time evolution of dilatation is similar to that of model 2a and time evolution of enstrophy is similar to that of model 2b. Turbulent kinetic energy is found to decay faster for model 2 than for model 1. This is similar to q^2 time evolution observed when models 1 and 2b are compared. Turbulence dissipation comparison is also similar to that between models 1 and 2b. Effects of vortex stretching, vortex dissipation and enstrophy-dilatation interaction are found to be larger for model 2 than for model 1. While effects of vortex stretching and dissipation for model 2 are similar to that of model 2b, the enstrophy-dilatation interaction transience is similar to that of model 2a. The energy spectra show larger dispersion of energy across the smaller length scales for model 2 than for model 1. This is consistent with the higher vortex stretching observed for model 2. model 2 has highest energy per wavenumber in the smaller length scales.

Time evolution of mean internal energy shows that the internal energy content for models 2a and 2 are much more when compared to those for models 1 and 2b. This is because for models 2a and 2, L.T.E. based thermodynamic properties are used.

λ , the Taylor microscale is representative of the turbulence length scales and η the Kol-

mogorov scale is representative of the dissipation length scales. Both λ and η are found to decrease slightly first and then increase at a constant rate. However the slope for η is larger than that of λ , thereby causing it to increase at a faster rate. This causes their ratio, λ/η to decrease with time. This ratio is representative of the range of length scales in the flow-field. Larger the range of length scales, stronger the process of cascading of turbulent kinetic energy from the turbulence length scales to the dissipation length scales. This ratio is the largest for model 2, followed by model 2b, then 2a and finally 1. This is consistent with the evolution of enstrophy observed for all models. Models 2 and 2b are observed to have the largest magnitude of vortex stretching and dissipation respectively, followed by models 2a and 1.

So, in general, dissipation is found to be affected by the transport properties and compressibility effects are found to be affected by the thermodynamic properties. The simulation results seem to suggest that model 2 which accounts for high temperature effects associated with both thermodynamic and transport properties should be chosen for simulating high temperature effects on decaying compressible isotropic turbulence accurately.

REFERENCES

1. **Aliseda, A., M. Bourgoïn, and E. Collaboration** (2014). Experimental study of homogeneous isotropic slowly-decaying turbulence in giant grid-wind tunnel set up. *67th Annual Meeting of the APS Divison of Fluid Dynamics*, **59**(20).
2. **Batchelor, G. and A. A. Townsend** (1947). Decay of vorticity in isotropic turbulence. *The Royal Society*, **190**(1023), 534–550.
3. **Batchelor, G. and A. A. Townsend** (1948). Decay of turbulence in the final period. *Proceedings of the Royal Society A*, **194**(1039), 527–543.
4. **Blaisdell, G. A.** (1991). *Numerical simulation of compressible homogeneous turbulence*. Ph.D. thesis, Stanford University.
5. **Boulos, M. I., P. Fauchais, and E. Pfender**, *Thermal Plasmas Fundamentals and Applications Volume 1*. Springer Science+Business Media LLC, 1994. ISBN 9781489913395.
6. **Chu, B.-T. and L. S. G. Kovasznay** (1958). Non-linear interactions in a viscous heat-conducting compressible gas. *Journal of Fluid Mechanics*, **3**(05), 494. ISSN 0022-1120.
7. **Comte-Bellot, G. and S. Corrsin** (1966). The use of a contraction to improve the isotropy of grid-generated turbulence. *Journal of Fluid Mechanics*, **25**(04), 657. ISSN 0022-1120.
8. **Corrsin, S.** (1952). Heat transfer in isotropic turbulence. *Journal of Applied Physics*, **23**(1), 113–118. ISSN 00218979.
9. **Erlebacher, G., M. Y. Hussaini, H. O. Kreiss, and S. Sarkar** (1990). The analysis and simulation of compressible turbulence. *Theoretical and Computational Fluid Dynamics*, **2**(2), 73–95. ISSN 09354964.
10. **G. A. Blaisdell, J. H. Q., E. T. Spyropoulos** (1996). The effect of the formulation of nonlinear terms on aliasing errors in spectral methods. *Applied Numerical Mathematics*, **21**(207-219).
11. **George, W. K.** (1992). The decay of homogeneous isotropic turbulence. *Physics of Fluids A*, **4**(7), 1492. ISSN 08998213.
12. **Ghosh, S. and K. Mahesh** (2008). Numerical simulation of the fluid dynamic effects of laser energy deposition in air. *Journal of Fluid Mechanics*, **605**, 329–354.
13. **Ghosh, S. and K. Mahesh** (2010). Dns of the thermal effects of laser energy deposition in isotropic turbulence. *Journal of Fluid Mechanics*, **654**, 387–416.
14. **Kovasznay, L. S. G.** (1953). Turbulence in supersonic flow.pdf. *Journal of Aeronautical Sciences*, **20**(10), 657–674.

15. **Ristorcelli, J. R.** and **G. A. Blaisdell** (1997). Consistent initial conditions for the DNS of compressible turbulence. *Physics of Fluids*, **4**(1997), 7–10.
16. **Rogallo, R. S.** (1981). Numerical Experiments in Homogeneous Turbulence. Technical report.
17. **Samtaney, R., D. I. Pullin,** and **B. Kosović** (2001). Direct numerical simulation of decaying compressible turbulence and shocklet statistics. *Physics of Fluids*, **13**(5), 1415–1430. ISSN 10706631.
18. **Sarkar, S.** and **M. Y. Hussaini** (1993). Computation of the sound generated by isotropic turbulence. *NASA STI/Recon Technical Report N*, **94**(1991), 30.
19. **Sutherland, W.** (1893). The viscosity of gases and molecular force. *Philosophical Magazine Series 5*, (36:223), 507–531.
20. **Tavoularis, S., J. C. Bennett,** and **S. Corrsin** (1978). Velocity-derivative skewness in small reynolds number, nearly isotropic turbulence. *Journal of Fluid Mechanics*, **88**, 63–69.
21. **Xinliang, L., F. Dexun,** and **M. Yanwen** (2002). Direct numerical simulation of compressible isotropic turbulence. *Science in China Series A: Mathematics*, **45**(11), 1452–1460.
22. **Zeman, O.** (1991). On the decay of isotropic turbulence. *Physics of Fluids A: Fluid Dynamics*, **3**(5), 951–955. ISSN 0022-1120.

LIST OF PAPERS BASED ON THESIS

1. Gokul Ramanathan and Shankar Ghosh DNS of high temperature effects on compressible isotropic turbulence *55th AIAA Aerospace Sciences Meeting, AIAA SciTech Forum and Exposition, 9th - 13th January, 2017 in Grapevine, Texas..*